Supplementary Information

Universal and Scalable Synthesis of Photochromic Single-Atom Catalysts for Plastic Recycling

Yu Liu,[1,#] Xuchun Wang,[1,2,#] Xiaodong Li,[3,#] Zuyang Ye,[4] Tsun-Kong Sham,[2] Panpan Xu,[5] Muhan Cao,[1] Qiao Zhang,[1] Yadong Yin,[4,] Jinxing Chen[1,*]*

[1] Institute of Functional Nano & Soft Materials (FUNSOM), Jiangsu Key Laboratory for Carbon-Based Functional Materials & Devices, Soochow University, Suzhou 215123, China

[2] Department of Chemistry, University of Western Ontario, London, Ontario N6A 5B7, Canada

[3] Max Planck Institute of Microstructure Physics, Weinberg 2, Halle 06120, Germany

[4] Department of Chemistry, University of California, Riverside, CA 92521, USA

[5] Advanced Materials Division, Suzhou Institute of Nano-Tech and Nano-Bionics, Chinese Academy of Sciences, Suzhou 215123, China

[#] These authors contributed equally to this work: Yu Liu, Xuchun Wang, Xiaodong Li

[*] These authors jointly supervised this work: Yadong Yin, Jinxing Chen

[*] Yadong Yin: yadong.yin@ucr.edu

[*] Jinxing Chen: chenjinxing@suda.edu.cn

Chemicals

All chemicals utilized in this experiment were of analytical grade and employed without additional purification. Titanium(IV) chloride ($TiCl_4$) liquid, manganese(II) chloride ($MnCl_2$) powder, zirconium(II) chloride ($ZrCl_2$) powder, tantalum(V) chloride ($TaCl_5$) powder, niobium(V) pentachloride ($NbCl_5$) powder, gallium(III) chloride ($GaCl_3$) powder, vanadium(III) chloride (VCl_3) powder, molybdenum oxide (MoO_3) powder, nickel oxide (NiO) powder were procured from Aladdin Ltd.; ruthenium(III) chloride powder, copper(II) chloride ($CuCl_2$) powder, cobalt(II) chloride hexahydrate ($CoCl_2{\cdot}6H_2O$) powder, nickel(II) chloride hexahydrate ($NiCl_2{\cdot}6H_2O$) powder, copper oxide (CuO) powder, diethylene glycol (DEG) liquid, ethylene glycol (EG) liquid were sourced from Sigma-Aldrich. The iron(III) chloride ($FeCl_3$) powder, iridium(III) chloride trihydrate ($IrCl_3{\cdot}3H_2O$) powder, tin(IV) chloride pentahydrate ($SnCl_4{\cdot}5H_2O$) powder, titanium dioxide (P25) powder were obtained from Acros Organics. Molybdenum(V) pentachloride ($MoCl_5$) powder, zinc(II) chloride ($ZnCl_2$) powder, Tricobalt tetraoxide (Co_3O_4) powder were acquired from Macklin (China). Chromium(III) chloride ($CrCl_3$) powder, deuterated dimethyl sulfoxide (d^6-DMSO) liquid were purchased from Energy Chemical Reagent (China). Palladium(II) chloride ($PdCl_2$) powder, tungsten(VI) chloride (WCl_6) powder were obtained from Strem Chemical Reagent (USA). Acetone was procured from Lingfeng Chemical Reagent (China). Poly(ethylene terephthalate) (PET) film (thickness = 25 microns), PET bottle, PET powder, polyethylene (PE) powder, polystyrene (PS) powder, poly (lactic acid) (PLA) tube, polycarbonate (PC) film sourced from Alibaba. Pristine PET, packaging film, bottles, dye-containing lunch boxes, multi-recycled waste, and bottle waste sourced from Taihu Lake. Ultra-pure deionized (DI) water (Milli-Q grade, 18.2 Ωm resistivity, TOC level <2 ppb) was directly obtained from a Milli-Q water purification system.

Characterizations

The crystalline structure and phase purity were determined using X-ray powder diffractometer using Cu Kα radiation (λ = 1.54056 Å) at 40 kV and 40 mA. Diffuse reflectance spectra (DRS) were collected using an ultraviolet-visible spectrophotometer (U-3900). The elemental composition of the M/TiO_2 nanostructures was characterized by inductively coupled plasma optical emission spectrometer (ICP-OES) analysis (PerkinElmer 8300). Before the analysis, the as-prepared oxide nanoparticles were dissolved in extra-pure hydrochloric acid. Thermogravimetric analysis (TGA) was performed on a Mettler Toledo Switzerland thermogravimetric analyzer from room temperature to 800 °C (ramping rate: 10 °C·min^{-1}) in an air atmosphere. Ultraviolet photoelectron spectroscopy (UPS) measurements were carried out in a custom-designed ultrahigh-vacuum system. He I (photon energy 21.22 eV) was used as the excitation source for UPS. Chemical compositions and valence states of all samples were analyzed using X-ray photoelectron spectroscopy (XPS) (Thermo Scientific ESCLAB Xi$^+$). All binding energies were calibrated by using the contaminant carbon (C *1s* = 284.8 eV) as a reference.

The sizes and morphologies of the M_1-TiO_2 were obtained on a ThermoFisher Talos F200X. The high-angle annular dark-field scanning TEM (HAADF-STEM) images and energy dispersive X-Ray spectroscopy (EDX) elemental mapping and Transmission electron microscopy (TEM) images were obtained with a Talos F200X instrument, both operated at a voltage of 200 kV. Aberration-corrected scanning transmission electron microscopy (AC-STEM) images and electron energy-loss spectroscopy (EELS) elemental mapping were obtained using a FEI Titan 80-300 S/TEM working at 300 kV with a probe spherical aberration corrector. Photographs were taken with a Canon 80D DSLR camera.

^{1}H nuclear magnetic resonance (NMR) spectra and ^{13}C NMR were acquired on a Bruker Advance III HD-400 MHz spectrometer and were analyzed using MestReNova (v11.0.1, Mestrelab Research S. L.). A BFO Smart Probe was used to enhance sensitivity. Chemical shifts (δ, ppm) were calibrated using the residual proton signals of the solvent and referenced to tetramethylsilane (TMS). The BHET was quantitatively analyzed using ^{1}H NMR spectroscopy at 400-MHz Bruker AVANCE AV III instrument, with d^6-dimethyl sulfoxide (d^6-DMSO) as the solution. The dichloromethane signals as internal standard (δ = 5.76 ppm, 1H), and the representative characteristic signals areas for BHET (δ = 8.13 ppm, 4H) were calculated to determine the yield of the BHET in the ^{1}H NMR spectra.

The yield of bis(2-hydroxyethyl) terephthalate (BHET) was analyzed using a Dionex HPLC-U3000 equipped with a C18 column (5 μm, 250 × 4.6 mm^2, Agilent) and an ultraviolet detector set at 254 nm. The mobile phase, a mixture of methanol and water (v/v = 50/50) was run for a duration of 20 min at a temperature of 30 °C, with a flow rate of 0.4 mL·min^{-1} and an injection volume of 15 μL.

Matrix-assisted laser desorption/ionization time of flight mass spectrometry (MALDI-TOF MS) was performed in reflector mode using a Bruker ultraflextreme MALDI-TOF/TOF instrument. Concentrated α-cyano-4-hydroxycinnamic acid (α-CHCA) in methanol was used as a matrix.

All solar experiments were performed under a solar simulator (CEL-HXF300-T3, Beijing China Education Au-light Co., Ltd.). The light intensity was calibrated by a CEAULIGHT: CEL-NP2000-2A solar power meter. The temperature of the reaction system was monitored by a JK804 multi-channel sensor.

The X-ray absorption fine structure (XAFS) spectra data, including X-ray absorption near-edge structure (XANES) and extended X-ray absorption fine structure (EXAFS) of Fe, Ti, Co, Ni, Cu, and Mo K-edges were collected at 44A beamline of Taiwan Photon Source (TPS) at the National Synchrotron Radiation Research Center (NSRRC), Taiwan. The XAFS data of the M_1-TiO_2 samples were performed at room temperature in transmission mode and the detectors were ionization-chamber-based. All the references (metal powder, foils, and oxide bulks) were recorded in the transmission mode using an ionization chamber. All the samples were pelletized as disks 13 mm in diameter with 1 mm thicknesses. Athena was used to calibrate and normalize the energy toward the X-ray absorption spectra (XAS) spectra. In the XANES fitting at K-edge, an arctangent background was subtracted from the normalized XANES spectra. In the EXAFS region of K-edge spectra, the k space was obtained by subtracting an arctangent background from the EXAFS spectra, and it was further converted into the R space through Fourier transform. Artemis was used to fit the EXAFS in R space.

DFT calculation details

Density functional theory (DFT) calculations were carried out on a Vienna Ab initio Simulation Package (VASP 5.4.4).[1] The exchange-correlation potential was described by the generalized gradient approximation (GGA) within the framework of Perdew-Burke-Ernzerhof (PBE) functional.[2] DFT-D3 method was employed to calculate the van der Waals (vdW) interaction.[3] Electronic energies were computed with the tolerance of 1×10^{-4} eV and total force of 0.02 eV·Å^{-1}. A kinetic cutoff energy of 450 eV was adopted. The crystal lattice parameters of TiO_2 bulk are as follows: a = b = 3.86205 Å, c = 9.69123 Å ($\alpha = \beta = \gamma = 90^{\circ}$). A Monkhorst-Pack k-mesh of 7 × 7 × 3 k-points were used in the structural relaxation for the bulk. The TiO_2 slabs were modeled by the corresponding exposed surface along (101) direction with the thickness of two-unit cells, in which three bottom atom layers are fixed to simulate the bulk structure. To avoid the interaction of the molecules on the surface, 5 × 4 TiO_2 supercell was built to provide enough surface space. The oxygen defect structure was simulated by removing one of the outermost oxygen atoms. A Monk Horst-Pack k-mesh of 1 × 1 × 1 k-points were used in the structural relaxation for all slab models. A vacuum space of 15 Å was inserted in z direction to avoid interactions between periodic images. The theoretical approach is based on the GGA with on-site Coulomb interaction parameter (GGA + U method), in which the effective U-J parameters of 4.2 and 4.0 eV were applied to improve the description of Ti and Fe *3d* states, respectively.[4-5]

Adsorption energies $E_{adsorption}$ are given with reference to the isolated surface $E_{surface}$ relaxed upon removing the molecule from the unit cell using identical computational parameters and the energy of the molecule $E_{molecule}$.

$$E_{adsorption} = E_{molecule\ on\ surface} - E_{surface} - E_{molecule} \tag{1}$$

The Gibbs free energy change (G) of reaction steps was calculated by the followings:

$$G = E_{DFT} + E_{ZPE} - TS \tag{2}$$

$$E_{ZPE} = \sum_i 1/2\ hv_i \tag{3}$$

$$\Theta_i = hv_i/k \tag{4}$$

$$S = \sum_i R[\ln\ (1 - e^{-\Theta_i/T})^{-1} + \frac{\Theta_i}{T}\ (e^{\frac{\Theta_i}{T}} - 1)^{-1}] \tag{5}$$

where E_{DFT} is the electronic energy calculated for specified geometrical structures, E_{ZPE} is the zero-point energy, S is the entropy, h is the Planck constant, v is the computed vibrational frequencies, Θ is the characteristic temperature of vibration, k is the Boltzmann constant, and R is the molar gas constant. For adsorbates, all 3N degrees of freedom were treated as frustrated harmonic vibrations with negligible contributions from the catalysts' surfaces.

The equilibrium concentration of point defects

The presence of point defects in the crystal, on the one hand, causes point distortions, which raise the internal energy of the crystal and reduce its thermodynamic stability; On the other hand, the increased disorder in the arrangement of the atoms and the change in the vibrational frequency of the atoms around them causes a change in the group and vibrational entropy, which increases the crystal entropy and increases the thermodynamic stability of the crystal. These two contradictory factors give the point defects in the crystal a certain equilibrium concentration at a certain temperature, which can be obtained according to thermodynamic theory. Using the vacancy as an example, the calculation process is as follows:

It is known from thermodynamic principles that at a constant temperature, the free energy of the whole system is F.

$$F = U - TS \tag{6}$$

In the equation, U is the internal energy, S is the total entropy value, including the group entropy (S_c) and the vibrational entropy (S_f), and T is the absolute temperature.

Supposed a crystal consisting of N atoms contains n vacancies. If the energy required to form a vacancy is E_v, the internal energy of the crystal will increase by nE_v when it contains n vacancies, and the change in the group entropy of the crystal caused by the vacancy is ΔS_c and the change in the vibrational entropy is $n\Delta S_f$. Thus, the change in free energy is:

$$\Delta F = nE_v - T(\Delta S_c + n\Delta S_f) \tag{7}$$

According to statistical thermodynamics, the group entropy can be expressed as

$$S_c = k \ln W \tag{8}$$

where k is the Boltzmann constant (1.38×10^{-23} J·K^{-1}) and W is the number of microstates so that the number of different arrangements possible in the presence of n vacancies and N atoms at the $N + n$ array positions:

$$W = \frac{(N+n)}{N!n!} \tag{10}$$

Thus, the increase in entropy of the crystal group state is given by:

$$\Delta S_c = k\left[\ln\frac{(N+n)!}{N!n!} - \ln 1\right] = k\ln\frac{(N+n)!}{N!n!} \tag{11}$$

When both N and n values are very large, the Stirling approximation formula can be used to change the above equation:

$$\Delta S_c = k[(N+n)\ln(N+n) - N\ln N - n\ln n] \tag{12}$$

Thus,

$$\Delta F = n\left(E_v - T\Delta S_f\right) - kT[(N+n)\ln(N+n) - N\ln N - n\ln n] \tag{13}$$

At equilibrium, the free energy is minimal,

$$\left(\frac{d\Delta F}{dn}\right)_T = 0 \tag{14}$$

$$\left(\frac{d\Delta F}{dn}\right)_T = E_v - T\Delta S_f - kT[\ln(N+n) - \ln n] = 0 \tag{15}$$

When $N >> n$,

$$\ln\frac{n}{N} \approx \frac{E_v - T\Delta S_f}{kT} \tag{16}$$

Equilibrium concentration of vacancies at temperature T,

$$\frac{n}{N} = exp\left(\frac{\Delta S_f}{k}\right) exp\,(\frac{-E_v}{kT}) = Aexp(\frac{-E_v}{kT}) \tag{17}$$

where A is the coefficient determined by the entropy of the vibration.

$$A = exp\left(\frac{\Delta S_f}{k}\right) \tag{18}$$

Therefore, the introduction of short-range order structures can release free energy of crystals, which is thermodynamically favorable for the synthesis of M_1-TiO_2 nanostructures.

Theory of GPA

The essence of geometric phase analysis (GPA) is the comparison of the phase of a set of perfect planes (defined by a g-vector) to the planes measured from an image (defined by a mask at the g-vector). If we consider and image to be formed from a Fourier series:

$$I(r) = \sum_g A_g e^{iP_g+2\pi i\boldsymbol{g}\cdot\boldsymbol{r}} \tag{19}$$

Where I is the image intensity, r is the position in the image and g are the periodicities in the image (i.e. the position in reciprocal space). A_g and P_g give the amplitude and phase of the periodicity given by g. Using a simple mask, it is easy to extract one (or a select few) of these Fourier components by masking the fast fourier transform (FFT). Inversing this FFT then produces the complex image. From this, the phase difference can be calculated as

$$P_g(\boldsymbol{r}) = Phase\left[H_g'(\boldsymbol{r})\right] - 2\pi\boldsymbol{g}\cdot\boldsymbol{r} \tag{20}$$

Where the first term is the phase from the masked FFT and the second term in the phase is calculated from the g-vector the FFT was masked at. At this point, the g-vector can be refined to an area of the homogeneous strain. If the g-vector is incorrect, (even if only by a little bit!) then the phase in the uniform strain region will have a gradient. By fitting this gradient, it is possible to correct the g-vector using

$$\Delta g = \frac{1}{2\pi}\nabla P_g \tag{21}$$

Each phase can be used to calculate the displacements in the direction of the lattice place. To get the full strain field, the phase needs to be calculated for two non-colinear g-vectors. The phases are related to the displacement field, u, by

$$\begin{pmatrix} P_{g1} \\ P_{g2} \end{pmatrix} = -2\pi\begin{pmatrix} g_{1x} & g_{1y} \\ g_{2x} & g_{2y} \end{pmatrix}\begin{pmatrix} u_x \\ u_{xy} \end{pmatrix} \tag{22}$$

Where g_{1x} and g_{1y} are the x and y components of the g-vector using to calculate the phase, P_{g1}. Inverting this gives the displacements in terms of the phases,

$$\begin{pmatrix} u_x \\ u_{xy} \end{pmatrix} = \frac{1}{-2\pi} \begin{pmatrix} a_{1x} & a_{2x} \\ a_{1y} & a_{2y} \end{pmatrix} \begin{pmatrix} P_{g1} \\ P_{g2} \end{pmatrix} \tag{23}$$

Where we have used

$$\begin{pmatrix} g_{1x} & g_{1y} \\ g_{2x} & g_{2y} \end{pmatrix}^T = \begin{pmatrix} a_{1x} & a_{2x} \\ a_{1y} & a_{2y} \end{pmatrix}^{-1} \tag{24}$$

Finally, the distortion is calculated by differentiating:

$$e = \begin{pmatrix} e_{xx} & e_{xy} \\ e_{yx} & e_{yy} \end{pmatrix} = \begin{pmatrix} \frac{\partial u_x}{\partial_x} & \frac{\partial u_x}{\partial_y} \\ \frac{\partial u_y}{\partial_x} & \frac{\partial u_y}{\partial_y} \end{pmatrix} \tag{25}$$

From this matrix, the strain, *ε*, rotation, *ω* and dilatation, *Δ*, are easily calculated from

$$\varepsilon = \frac{1}{2}(e + e^T) \tag{26}$$

$$\omega = \frac{1}{2}(e - e^T) \tag{27}$$

$$\Delta = Trace[e] \tag{28}$$

Note: the above discussion is based on the Cayman theme by Jason Long (http://jjppeters.github.io/Strainpp/)

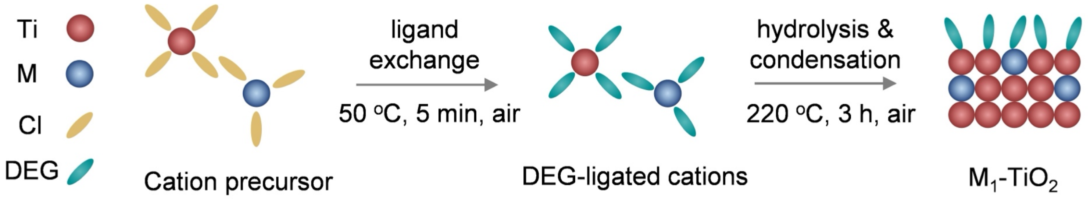

Supplementary Fig. 1 Schematics of M_1-TiO_2 nanostructures synthesis via diethylene glycol (DEG)-assisted method.

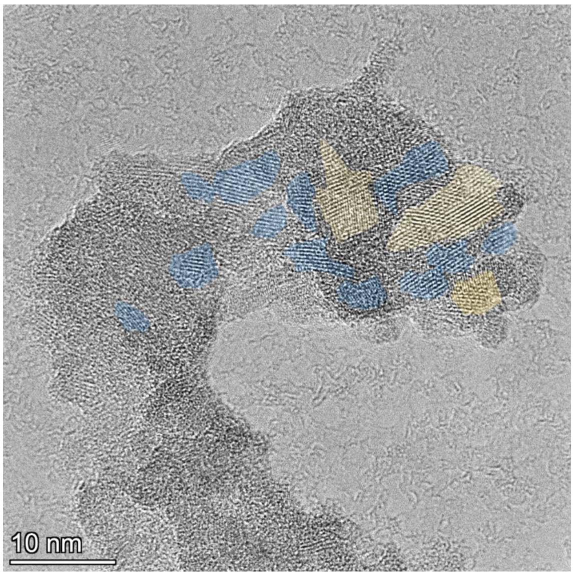

Supplementary Fig. 2 High resolution transmission electron microscope (HRTEM) image of Fe_1-TiO_2 nanostructures. The yellow and blue regions demonstrate that Fe_1-TiO_2 is polycrystalline, and the crystal domains are surrounded by amorphous TiO_2, forming crystal domains.

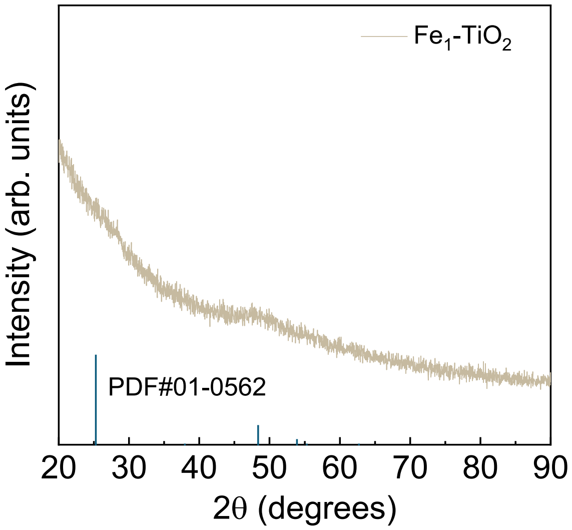

Supplementary Fig. 3 X-ray diffractometer (XRD) pattern of Fe$_1$-TiO$_2$ nanostructures. Source data are provided as a Source Data file.

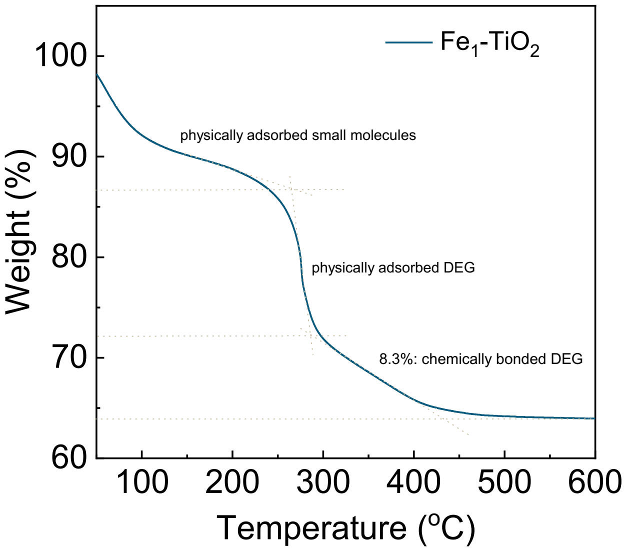

Supplementary Fig. 4 Thermogravimetric analysis (TGA) curve of Fe_1-TiO_2 in air with a heating rate of 10 °C·min^{-1}. Source data are provided as a Source Data file.

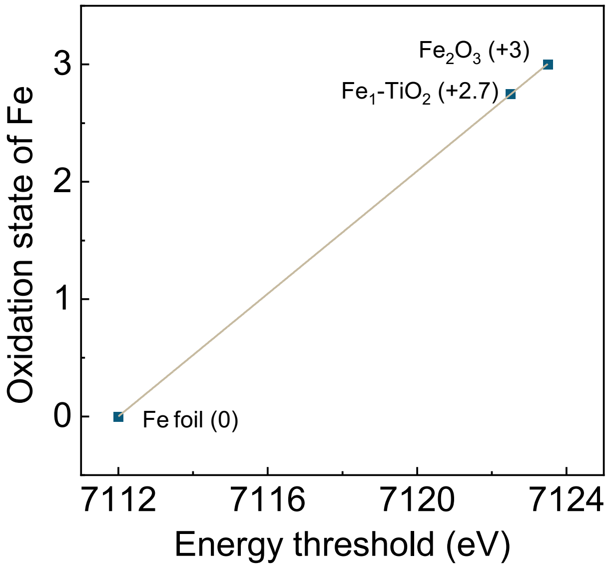

Supplementary Fig. 5 Plot of oxidation states of Fe in Fe$_1$-TiO$_2$ and references as determined from the edge positions in the Fe K-edge X-ray absorption near-edge structure (XANES) spectra. Source data are provided as a Source Data file.

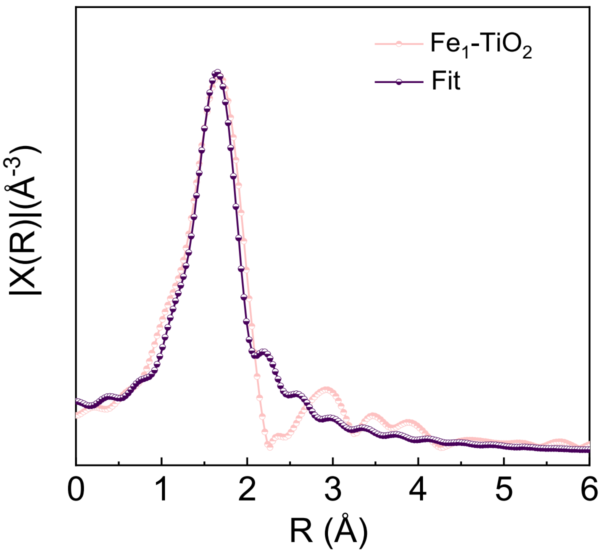

Supplementary Fig. 6 Fourier transforms of the extended X-ray absorption fine structure (FT-EXAFS) spectra of Fe_1-TiO_2 nanostructures and the theoretical fitted curve. Source data are provided as a Source Data file.

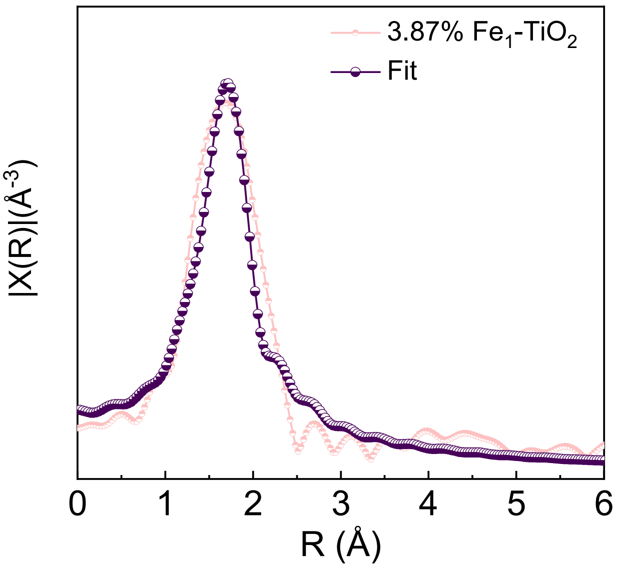

Supplementary Fig. 7 Fourier transforms of the extended X-ray absorption fine structure (FT-EXAFS) spectra of 3.87 at.% Fe_1-TiO_2 nanostructures and the theoretical fitted curve. Source data are provided as a Source Data file.

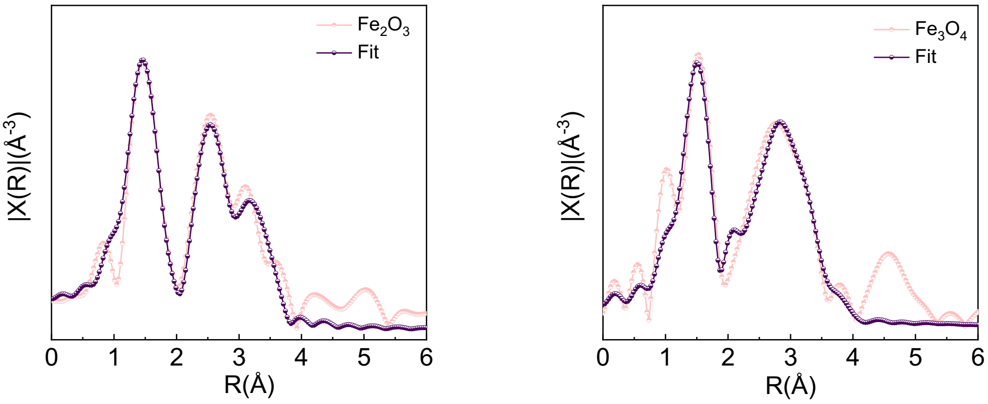

Supplementary Fig. 8 Fourier transforms of the extended X-ray absorption fine structure (FT-EXAFS) spectra of Fe_2O_3 and Fe_3O_4 and their theoretical fitted curves. Source data are provided as a Source Data file.

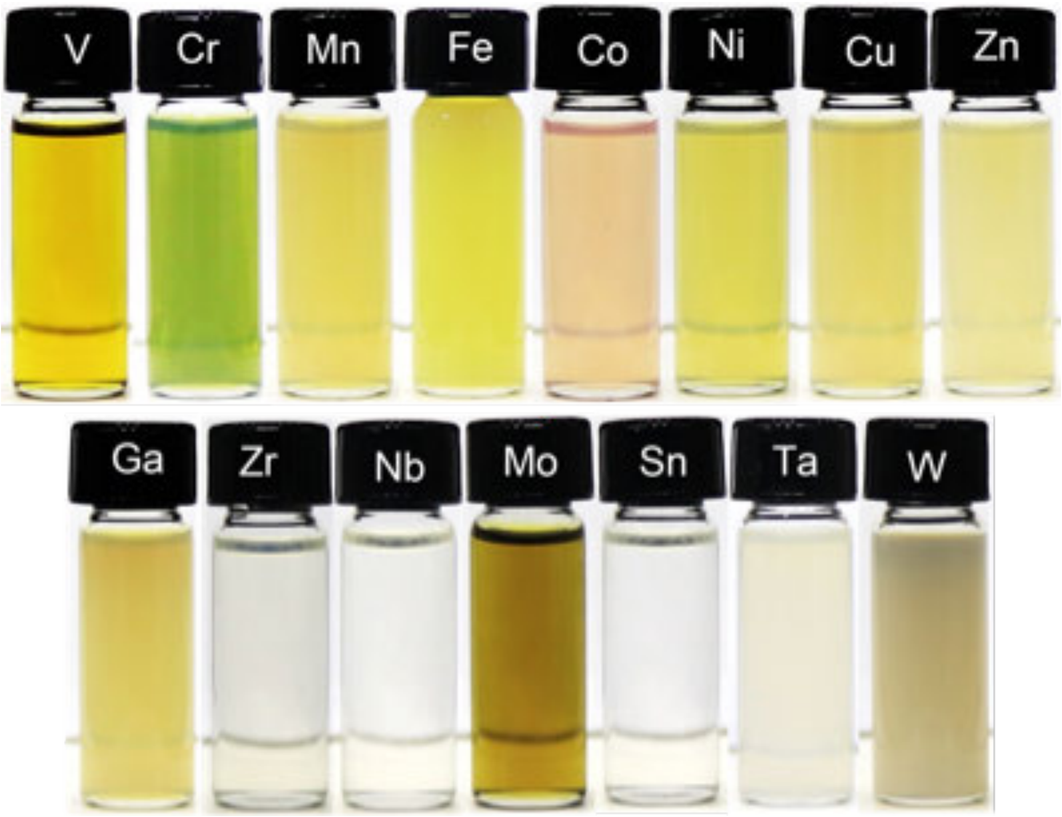

Supplementary Fig. 9 Diverse M_1-TiO_2 nanostructures synthesized by diethylene glycol (DEG)-assisted strategy.

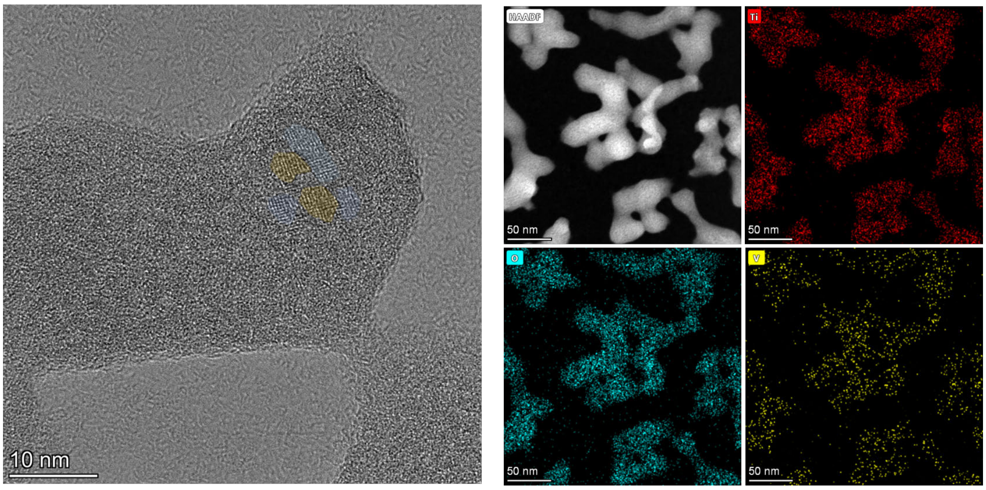

Supplementary Fig. 10 High resolution transmission electron microscope (HRTEM), scanning transmission electron microscopy (STEM) image and corresponding energy dispersive X-ray spectroscopy (EDX) elemental mapping images of V_1-TiO_2. The yellow and blue regions represent crystal domains.

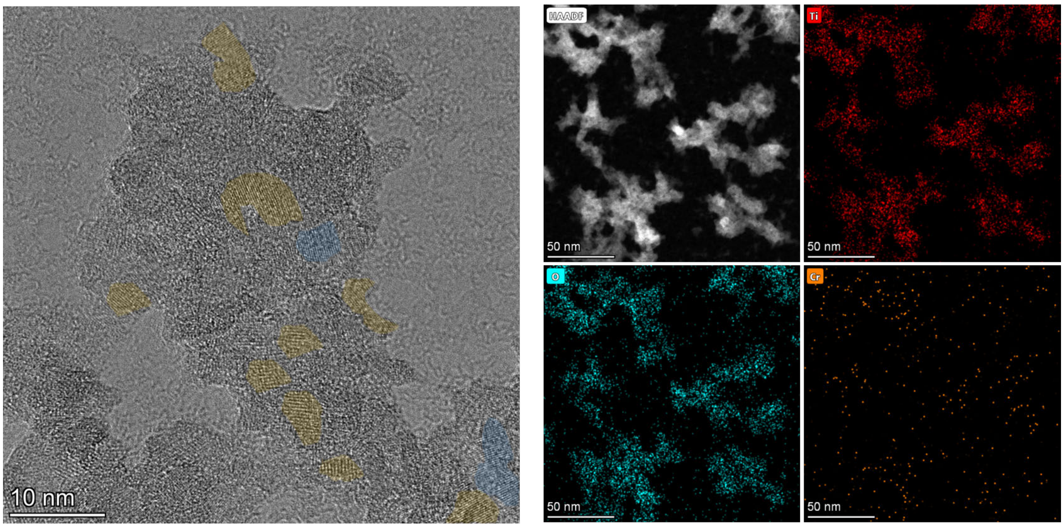

Supplementary Fig. 11 High resolution transmission electron microscope (HRTEM), scanning transmission electron microscopy (STEM) image and corresponding energy dispersive X-ray spectroscopy (EDX) elemental mapping images of Cr_1-TiO_2. The yellow and blue regions represent crystal domains.

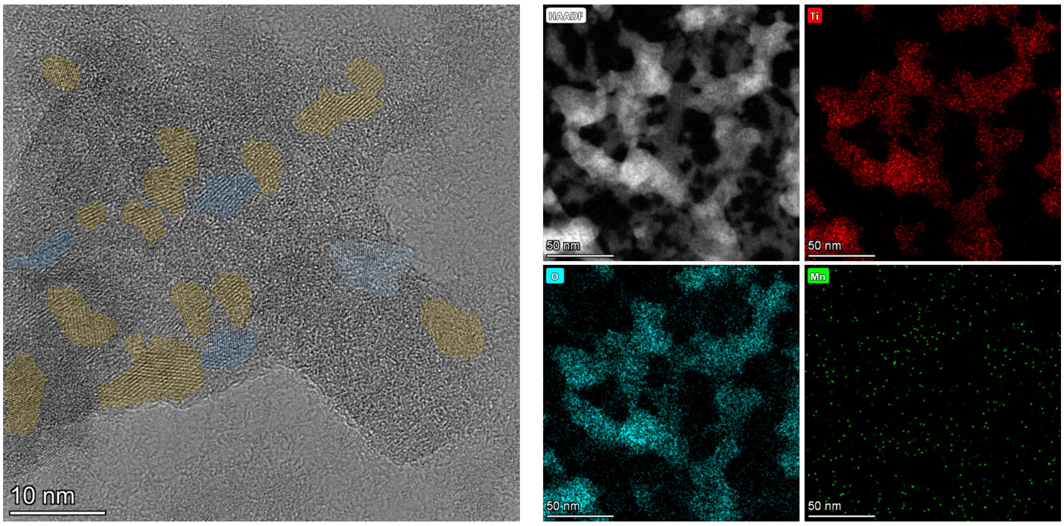

Supplementary Fig. 12 High resolution transmission electron microscope (HRTEM), scanning transmission electron microscopy (STEM) image and corresponding energy dispersive X-ray spectroscopy (EDX) elemental mapping images of Mn_1-TiO_2. The yellow and blue regions represent crystal domains.

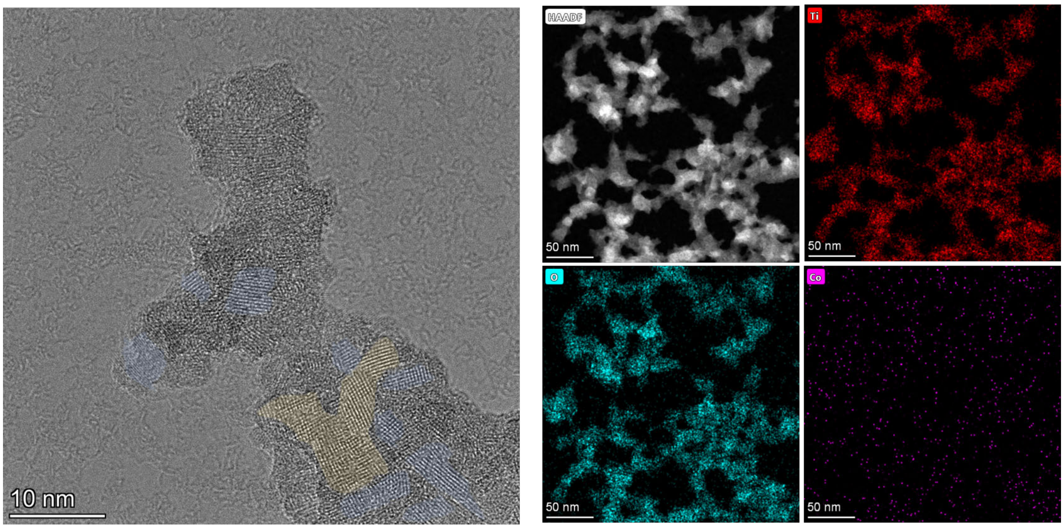

Supplementary Fig. 13 High resolution transmission electron microscope (HRTEM), scanning transmission electron microscopy (STEM) image and corresponding energy dispersive X-ray spectroscopy (EDX) elemental mapping images of Co_1-TiO_2. The yellow and blue regions represent crystal domains.

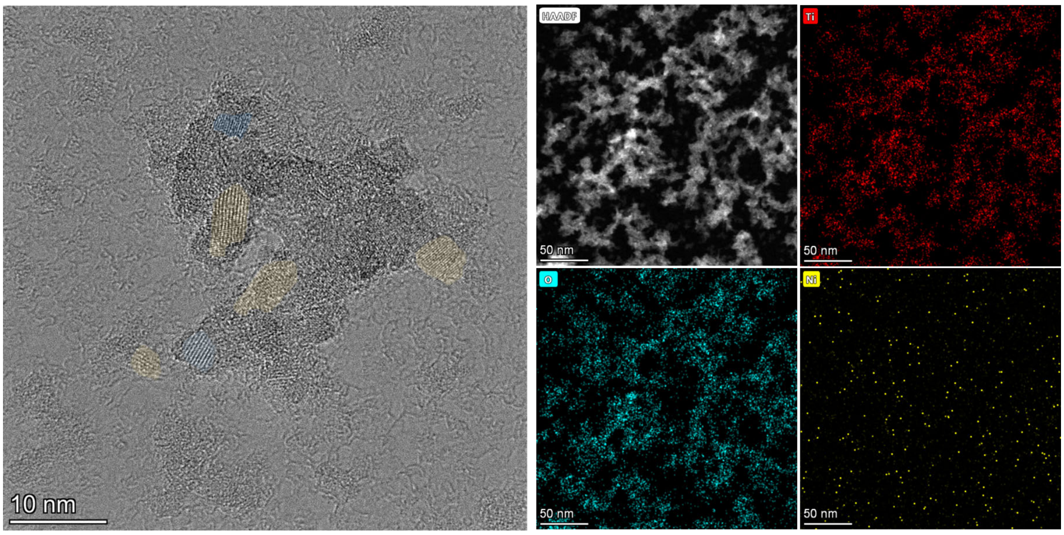

Supplementary Fig. 14 High resolution transmission electron microscope (HRTEM), scanning transmission electron microscopy (STEM) image and corresponding energy dispersive X-ray spectroscopy (EDX) elemental mapping images of Ni_1-TiO_2. The yellow and blue regions represent crystal domains.

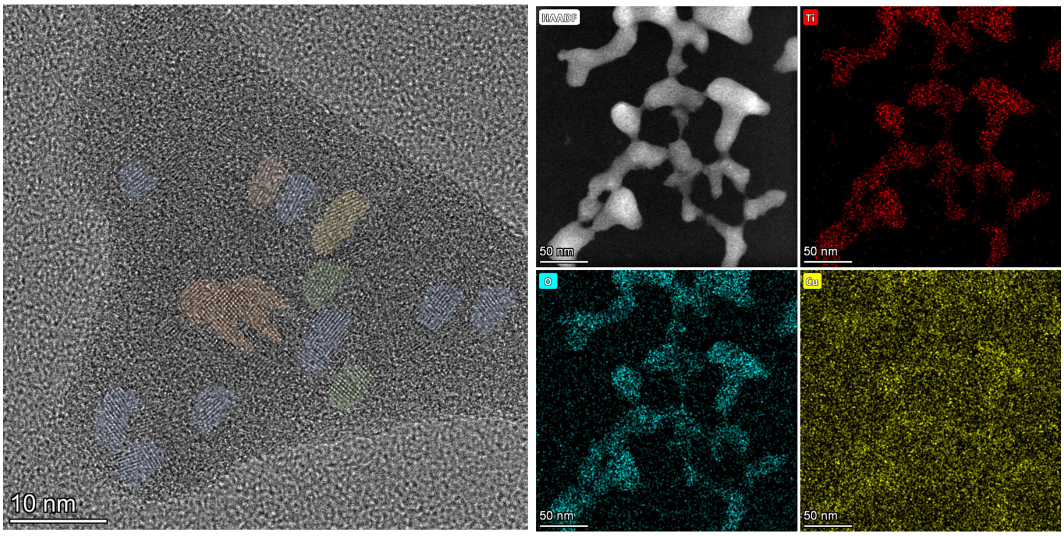

Supplementary Fig. 15 High resolution transmission electron microscope (HRTEM), scanning transmission electron microscopy (STEM) image and corresponding energy dispersive X-ray spectroscopy (EDX) elemental mapping images of Cu_1-TiO_2. The yellow and blue regions represent crystal domains.

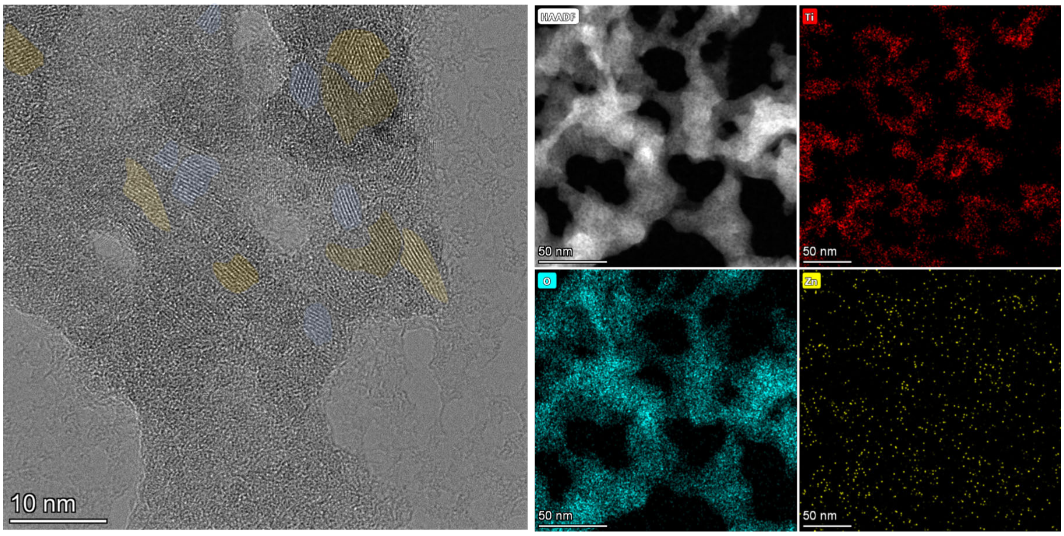

Supplementary Fig. 16 High resolution transmission electron microscope (HRTEM), scanning transmission electron microscopy (STEM) image and corresponding corresponding energy dispersive X-ray spectroscopy (EDX) elemental mapping images of Zn$_1$-TiO$_2$. The yellow and blue regions represent crystal domains.

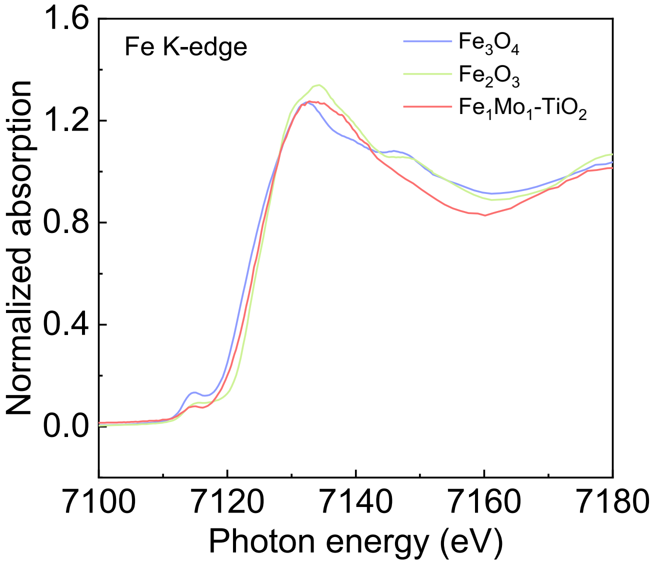

Supplementary Fig. 17 Fe K-edge normalized X-ray absorption near-edge structure (XANES) spectra of Fe$_1$Mo$_1$-TiO$_2$ and references. Source data are provided as a Source Data file.

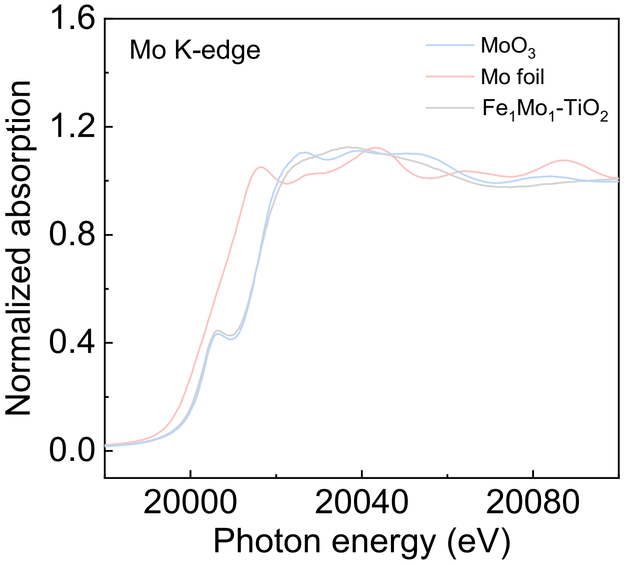

Supplementary Fig. 18 Mo K-edge normalized X-ray absorption near-edge structure (XANES) spectra of Fe_1Mo_1-TiO_2 and references. Source data are provided as a Source Data file.

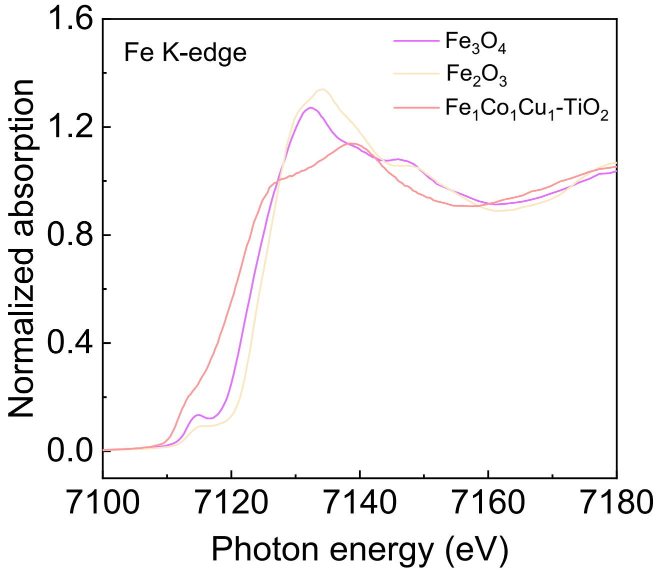

Supplementary Fig. 19 Fe K-edge normalized X-ray absorption near-edge structure (XANES) spectra of Fe$_1$Co$_1$Cu$_1$-TiO$_2$ and references. Source data are provided as a Source Data file.

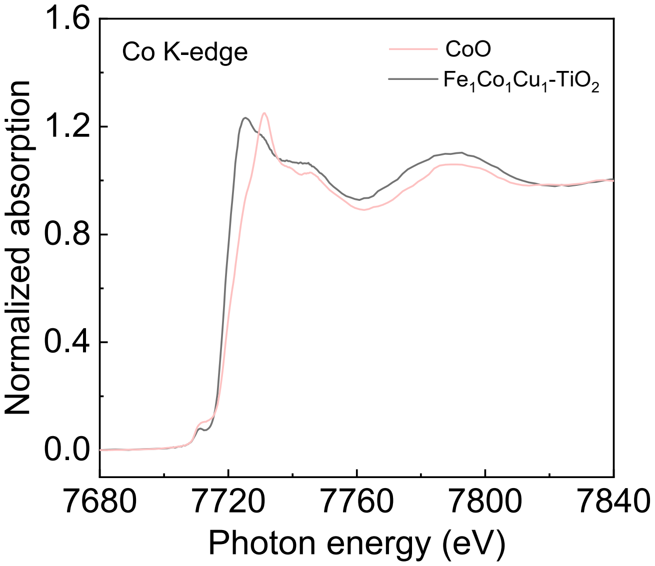

Supplementary Fig. 20 Co K-edge normalized X-ray absorption near-edge structure (XANES) spectra of $Fe_1Co_1Cu_1$-TiO_2 and reference. Source data are provided as a Source Data file.

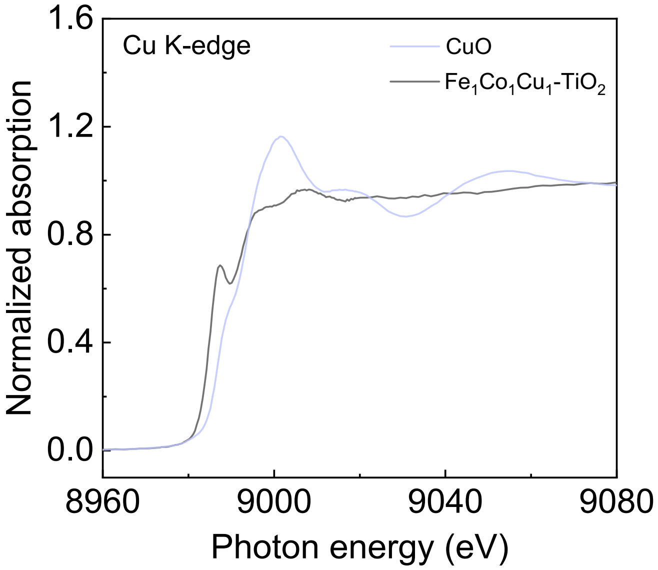

Supplementary Fig. 21 Cu K-edge normalized X-ray absorption near-edge structure (XANES) spectra of $Fe_1Co_1Cu_1$-TiO_2 and reference. Source data are provided as a Source Data file.

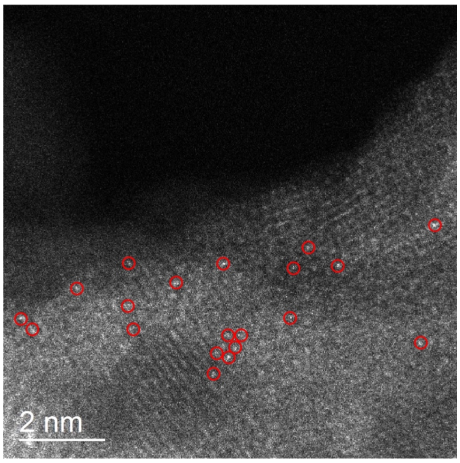

Supplementary Fig. 22 Aberration-corrected high-angle annular dark-field scanning transmission electron microscopy (AC-HAADF-STEM) image of Fe_1Mo_1-TiO_2 nanostructures. Marked the Mo atoms with a bright red circle.

To further enhance the credibility of our product characterization, we supplemented with Aberration-corrected high-angle annular dark-field scanning transmission electron microscopy (AC-HAADF-STEM) characterization. As is well known, AC-HAADF-STEM is the most intuitive method for confirming the presence of isolated metal single atoms, relying on Rutherford scattering. This technique is highly sensitive to variations in the atomic number of atoms in the sample (Z-contrast images), where the image intensity of a specific atom is directly proportional to the square of the elemental atomic number (Z^2). In essence, the higher the Z value of an element, the brighter its image appears. In this work, direct observation by AC-HAADF-STEM is challenging due to the majority of heteroatoms' atomic numbers being close to that of Ti. Given the substantial difference in atomic numbers between Mo ($Z = 42$) and Ti ($Z = 22$), Fe_1Mo_1-TiO_2 catalysts were selected as a representative sample for AC-HAADF-STEM characterization, where Mo in Fe_1Mo_1-TiO_2 exists in an atomically dispersed state (marked with bright red circles).

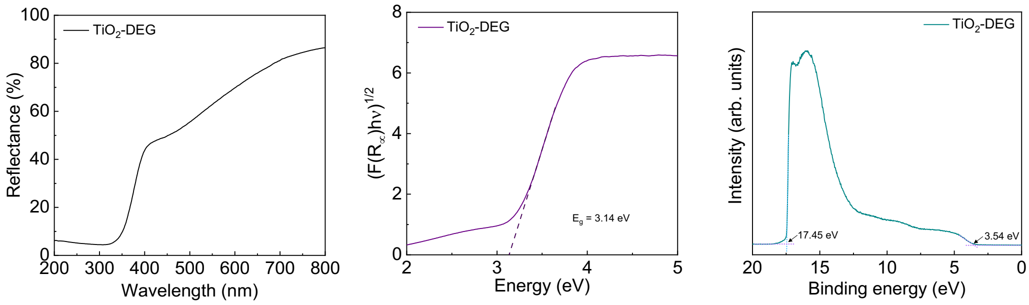

Supplementary Fig. 23 UV–vis diffuse reflectance spectrum (DRS), band gap energy (E_g) spectrum, and ultraviolet photoelectron spectroscopy (UPS) analysis for valence-band regions of TiO_2-DEG. Source data are provided as a Source Data file.

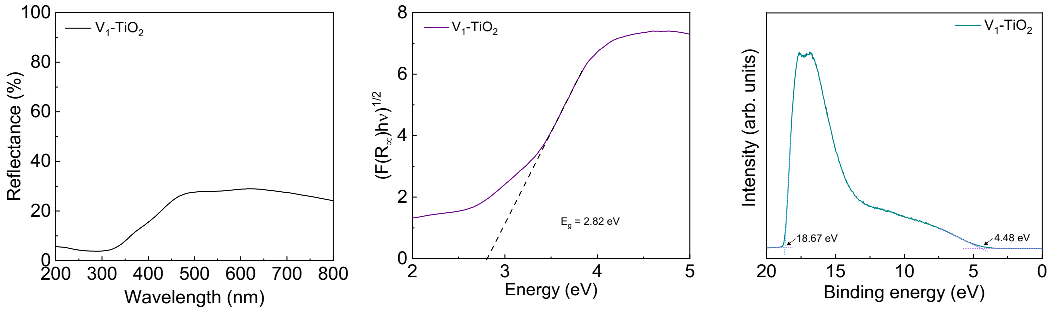

Supplementary Fig. 24 UV–vis diffuse reflectance spectrum (DRS), band gap energy (E_g) spectrum, and ultraviolet photoelectron spectroscopy (UPS) analysis for valence-band regions of V_1-TiO_2. Source data are provided as a Source Data file.

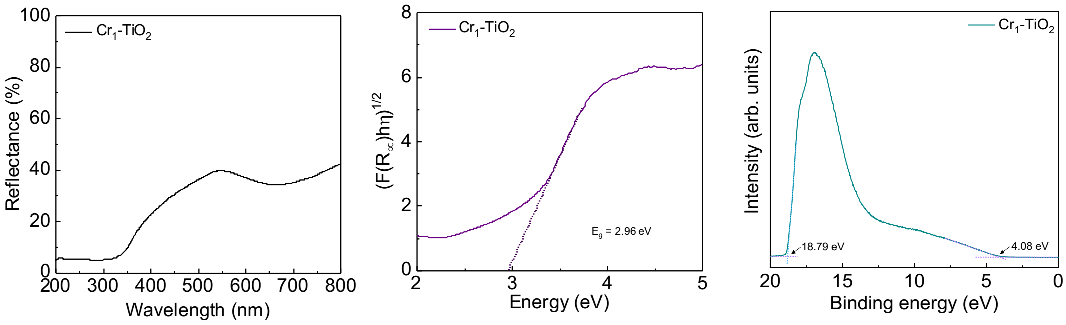

Supplementary Fig. 25 UV–vis diffuse reflectance spectrum (DRS), band gap energy (E_g) spectrum, and ultraviolet photoelectron spectroscopy (UPS) analysis for valence-band regions of Cr$_1$-TiO$_2$. Source data are provided as a Source Data file.

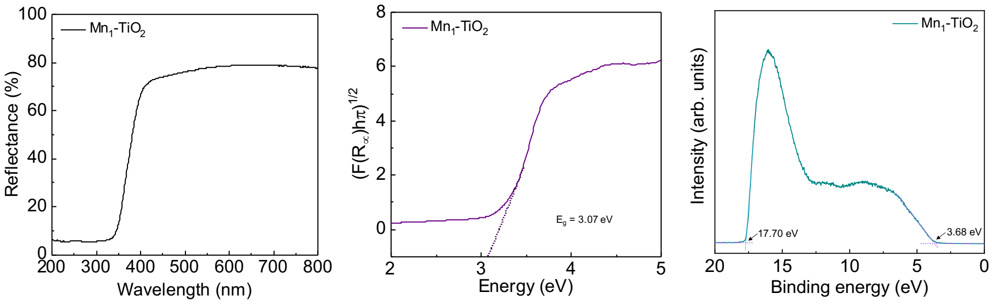

Supplementary Fig. 26 UV–vis diffuse reflectance spectrum (DRS), band gap energy (E_g) spectrum, and ultraviolet photoelectron spectroscopy (UPS) analysis for valence-band regions of Mn_1-TiO_2. Source data are provided as a Source Data file.

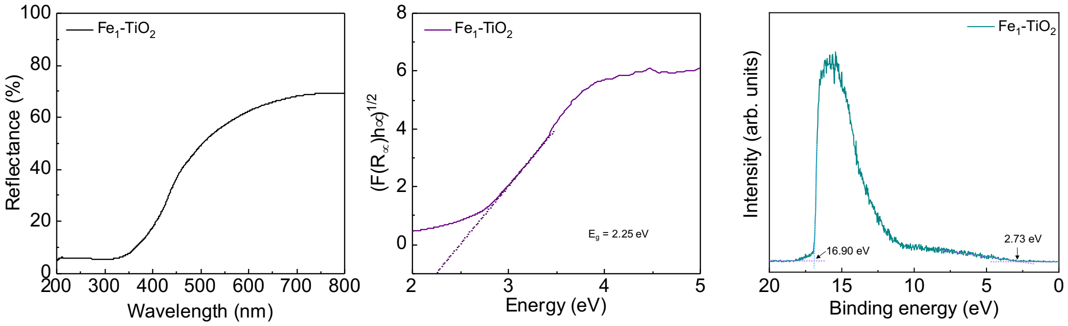

Supplementary Fig. 27 UV–vis diffuse reflectance spectrum (DRS), band gap energy (E_g) spectrum, and ultraviolet photoelectron spectroscopy (UPS) analysis for valence-band regions of Fe$_1$-TiO$_2$. Source data are provided as a Source Data file.

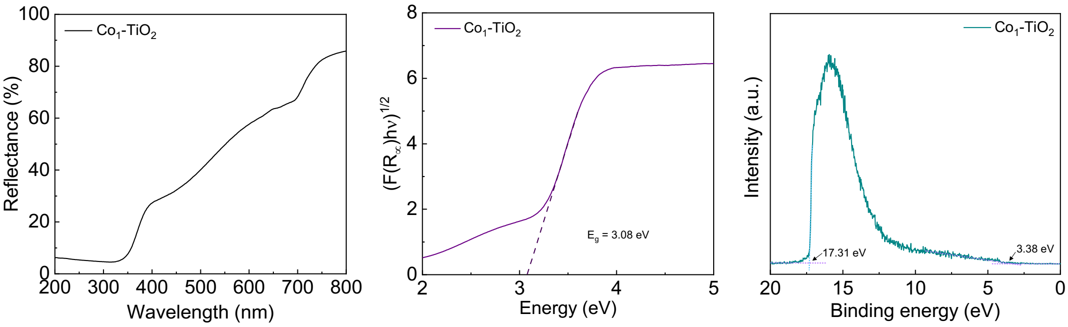

Supplementary Fig. 28 UV–vis diffuse reflectance spectrum (DRS), band gap energy (E_g) spectrum, and ultraviolet photoelectron spectroscopy (UPS) analysis for valence-band regions of Co$_1$-TiO$_2$. Source data are provided as a Source Data file.

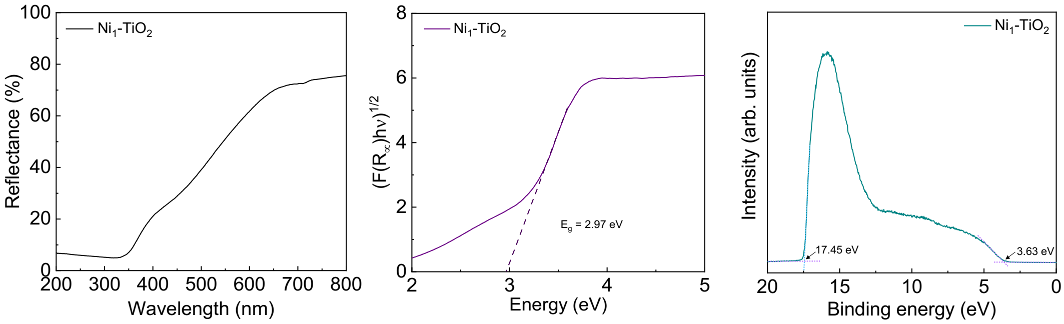

Supplementary Fig. 29 UV–vis diffuse reflectance spectrum (DRS), band gap energy (E_g) spectrum, and ultraviolet photoelectron spectroscopy (UPS) analysis for valence-band regions of Ni$_1$-TiO$_2$. Source data are provided as a Source Data file.

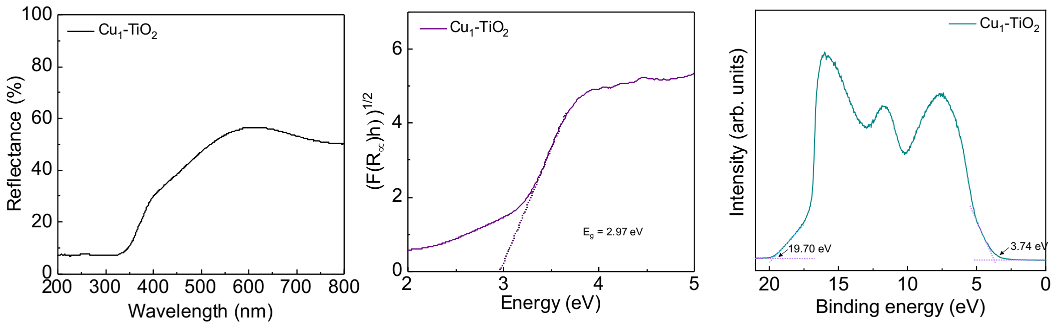

Supplementary Fig. 30 UV–vis diffuse reflectance spectrum (DRS), band gap energy (E_g) spectrum, and ultraviolet photoelectron spectroscopy (UPS) analysis for valence-band regions of Cu$_1$-TiO$_2$. Source data are provided as a Source Data file.

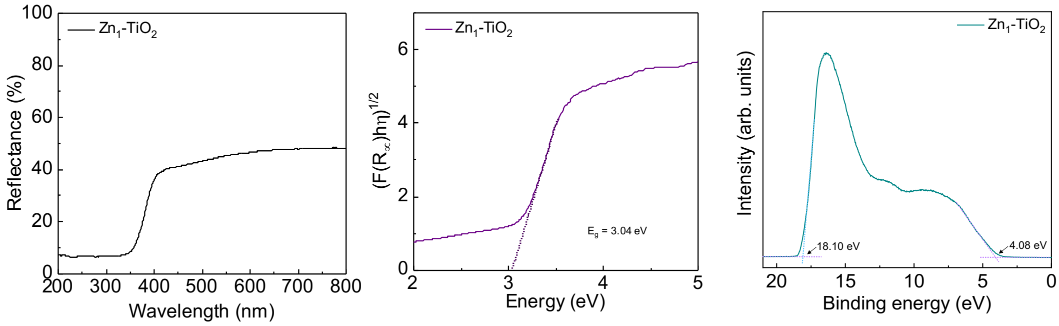

Supplementary Fig. 31 UV–vis diffuse reflectance spectrum (DRS), band gap energy (E_g) spectrum, and ultraviolet photoelectron spectroscopy (UPS) for valence-band regions of Zn$_1$-TiO$_2$. Source data are provided as a Source Data file.

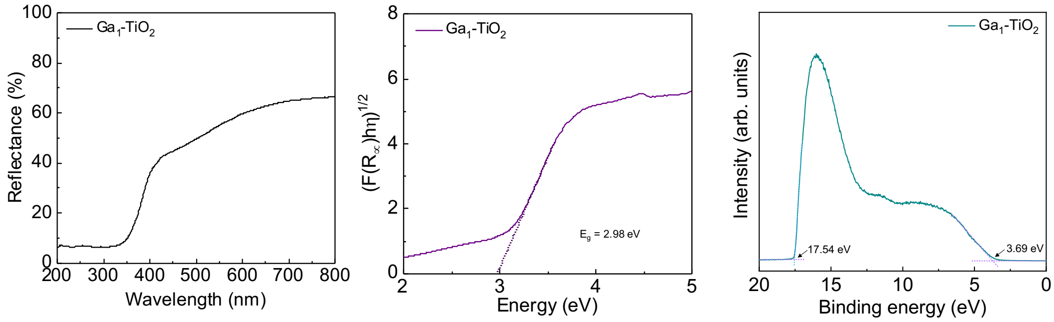

Supplementary Fig. 32 UV–vis diffuse reflectance spectrum (DRS), band gap energy (E_g) spectrum, and ultraviolet photoelectron spectroscopy (UPS) analysis for valence-band regions of Ga$_1$-TiO$_2$. Source data are provided as a Source Data file.

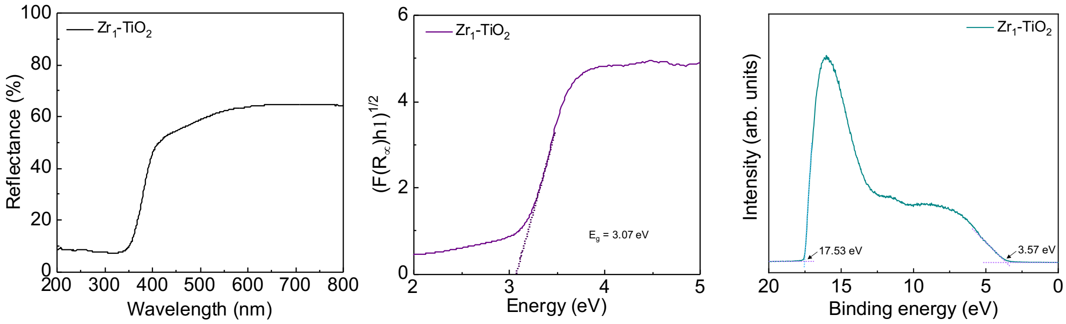

Supplementary Fig. 33 UV–vis diffuse reflectance spectrum (DRS), band gap energy (E_g) spectrum, and ultraviolet photoelectron spectroscopy (UPS) analysis for valence-band regions of Zr$_1$-TiO$_2$. Source data are provided as a Source Data file.

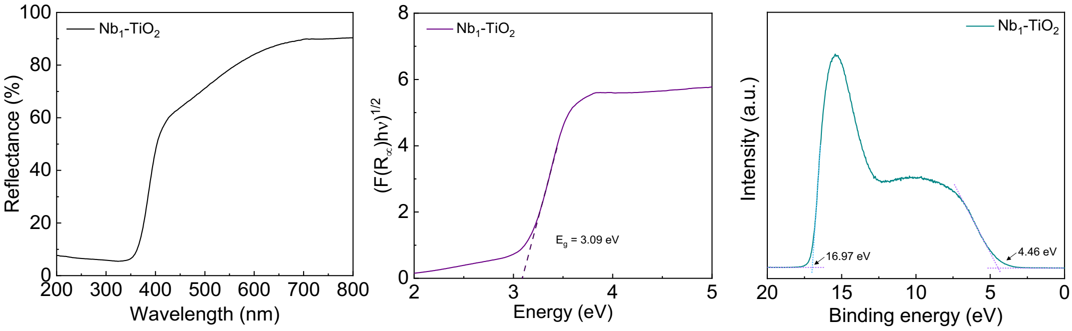

Supplementary Fig. 34 UV–vis diffuse reflectance spectrum (DRS), band gap energy (E_g) spectrum, and ultraviolet photoelectron spectroscopy (UPS) analysis for valence-band regions of Nb$_1$-TiO$_2$. Source data are provided as a Source Data file.

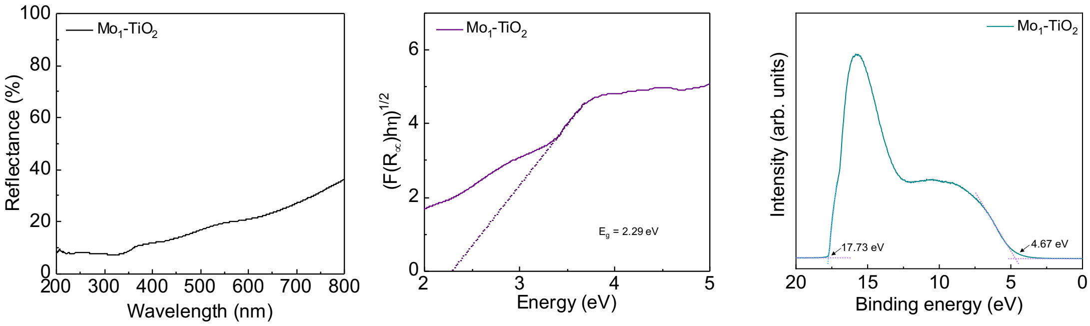

Supplementary Fig. 35 UV–vis diffuse reflectance spectrum (DRS), band gap energy (E_g) spectrum, and ultraviolet photoelectron spectroscopy (UPS) analysis for valence-band regions of Mo_1-TiO_2. Source data are provided as a Source Data file.

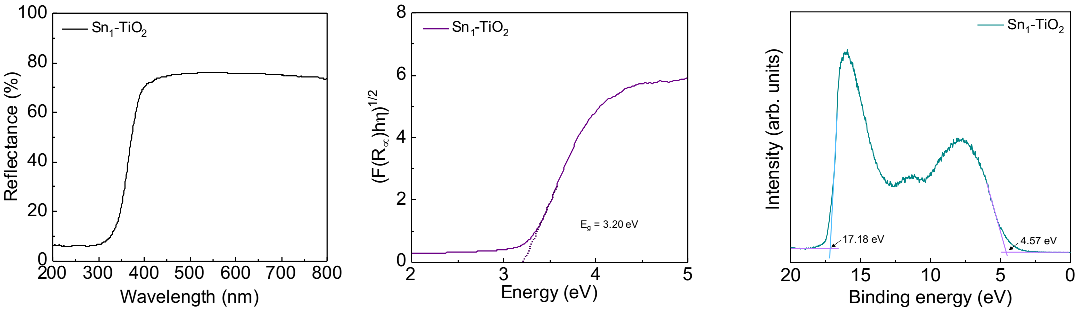

Supplementary Fig. 36 UV–vis diffuse reflectance spectrum (DRS), band gap energy (E_g) spectrum, and ultraviolet photoelectron spectroscopy (UPS) analysis for valence-band regions of Sn$_1$-TiO$_2$. Source data are provided as a Source Data file.

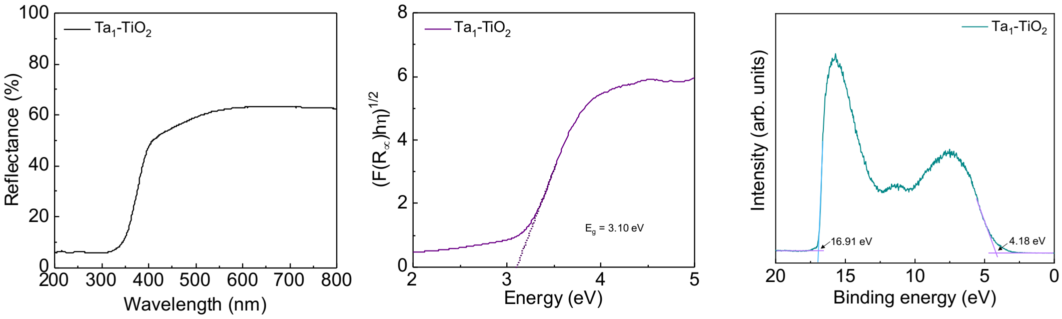

Supplementary Fig. 37 UV–vis diffuse reflectance spectrum (DRS), band gap energy (E_g) spectrum, and ultraviolet photoelectron spectroscopy (UPS) analysis for valence-band regions of Ta$_1$-TiO$_2$. Source data are provided as a Source Data file.

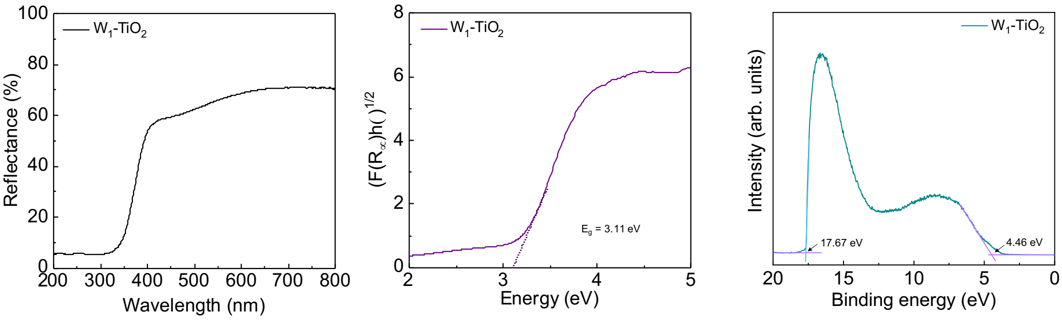

Supplementary Fig. 38 UV–vis diffuse reflectance spectrum (DRS), band gap energy (E_g) spectrum, and ultraviolet photoelectron spectroscopy (UPS) analysis for valence-band regions of W$_1$-TiO$_2$. Source data are provided as a Source Data file.

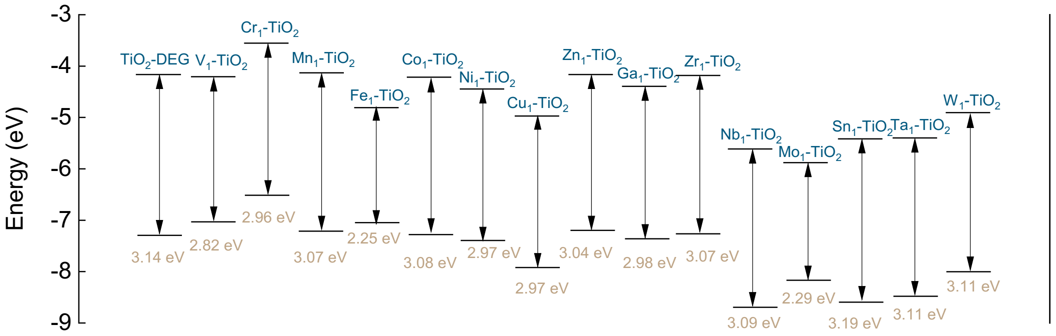

Supplementary Fig. 39 Summarized energy band structure of various M$_1$-TiO$_2$. Source data are provided as a Source Data file.

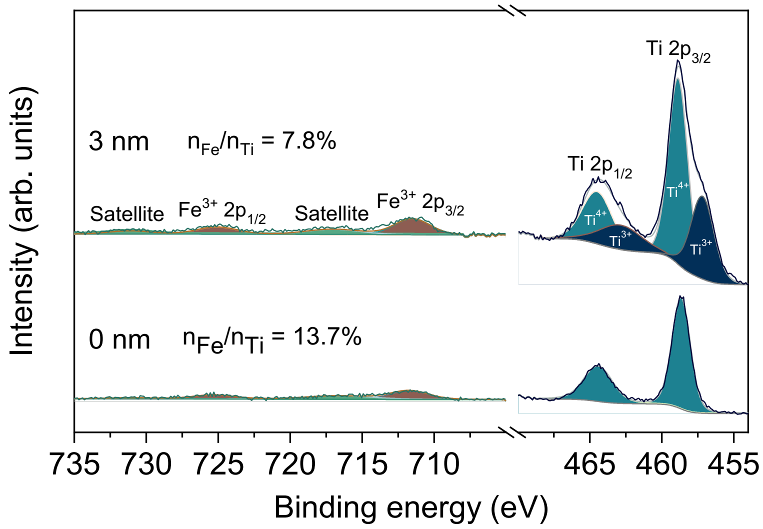

Supplementary Fig. 40 Depth-dependent high-resolution Fe *2p* and Ti *2p* X-ray photoelectron spectroscopy (XPS) spectra of Fe_1-TiO_2. Source data are provided as a Source Data file.

X-ray photoelectron spectroscopy (XPS) depth profiling uses an ion beam to etch surface layers, revealing structural information at different depths. the Fe-Ti atomic ratio on the catalyst surface is 13.7%, which decreases with the increase of etching depth. The Fe-Ti atomic ratio decreases to 7.8% when the etching depth is ~3 nm. These results confirm the ability of this technique to prepare M_1-TiO_2 catalysts with a surface rich in heteroatoms.

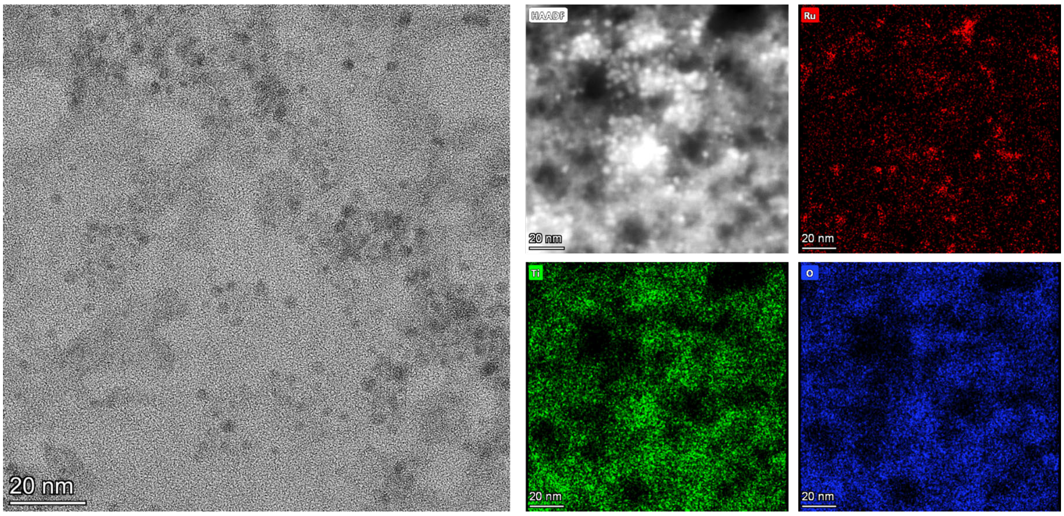

Supplementary Fig. 41 Transmission electron microscope (TEM), scanning transmission electron microscopy (STEM) image and corresponding corresponding energy dispersive X-ray spectroscopy (EDX) elemental mapping images of 5 at.%Ru-TiO_2.

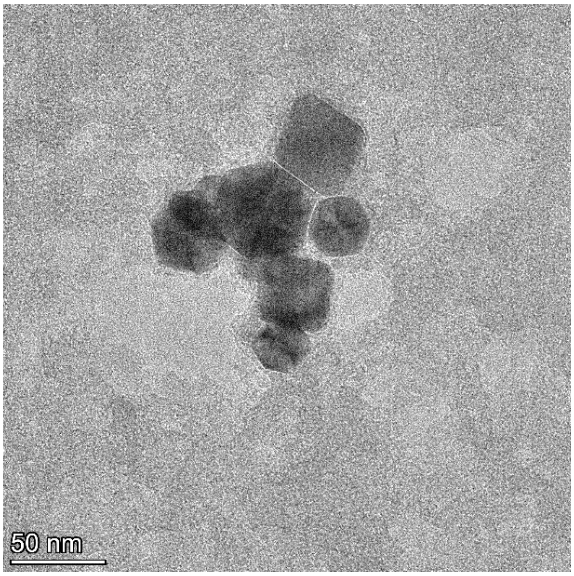

Supplementary Fig. 42 Transmission electron microscope (TEM) image of 5 at.%Pd-TiO_2.

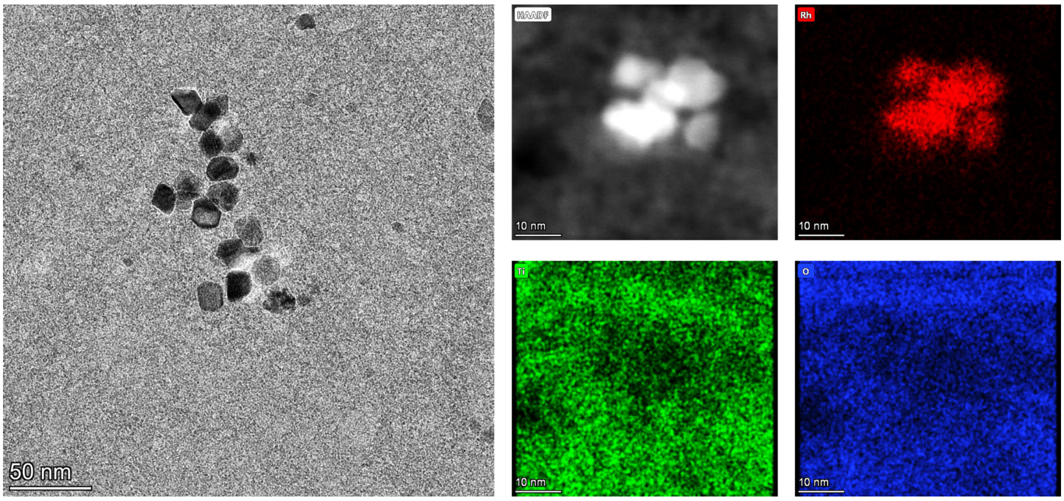

Supplementary Fig. 43 Transmission electron microscope (TEM), scanning transmission electron microscopy (STEM) image and corresponding corresponding energy dispersive X-ray spectroscopy (EDX) elemental mapping images of 5 at.%Rh-TiO_2.

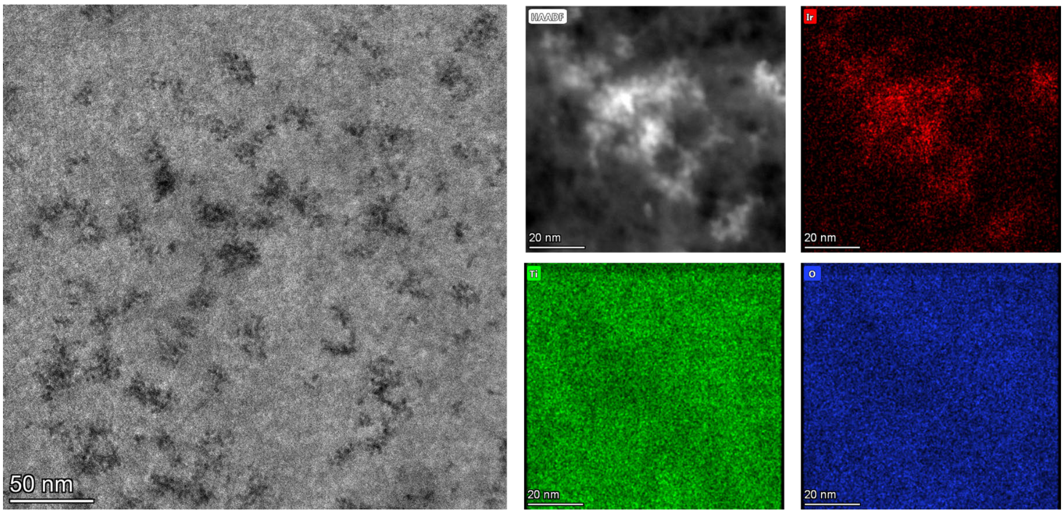

Supplementary Fig. 44 Transmission electron microscope (TEM), scanning transmission electron microscopy (STEM) image and corresponding energy dispersive X-ray spectroscopy (EDX) elemental mapping images of 5 at.%Ir-TiO_2.

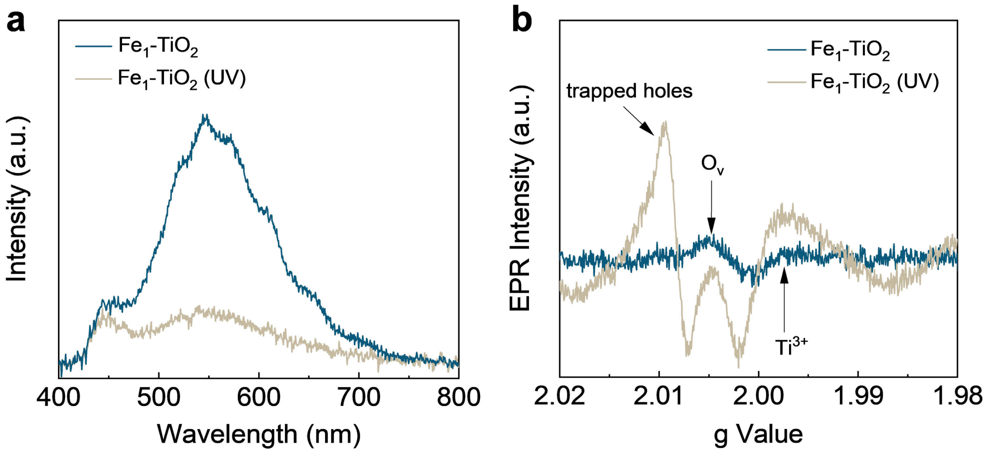

Supplementary Fig. 45 (a) Photoluminescence and (b) electron paramagnetic resonance (EPR) spectra of Fe_1-TiO_2 nanostructures before and after ultraviolet light (UV) exposure for 30 min. Source data are provided as a Source Data file.

In the photothermal polyester upcycling, when the Fe_1-TiO_2 catalysts are exposed to simulated sunlight, they are excited by high-energy UV photons. This excitation leads to the generation of electron-hole pairs. The chemical-bonded diethylene glycol (DEG) ligand effectively captures the holes, thus extending the electron lifetime by preventing rapid carrier recombination (*Angew. Chem. Int. Ed. 2023, 135, e202308930*). Following ultraviolet light (UV) irradiation, there is a significant decrease in the photoluminescence intensity of the Fe_1-TiO_2 catalysts. This decrease is attributed to the catalyst's black color in its active state, which harbors abundant defect energy levels. These defects facilitate non-radiative carrier relaxation when the excitation light interacts with the catalyst's surface, leading to diminished fluorescence intensity. Further, the absorption spectrum reveals enhanced absorption of visible light, corroborating this observation. Moreover, the longevity of the electron aids in the reduction of Ti^{4+} within the Fe_1-TiO_2 catalysts to Ti^{3+} species, simultaneously generating oxygen vacancies. There is a dramatic increase in the count of Ti^{3+} and O_v in the electron paramagnetic resonance (EPR) spectra after UV irradiation. This finding suggests that the photogenerated carriers interact primarily with the Fe_1-TiO_2 catalyst itself.

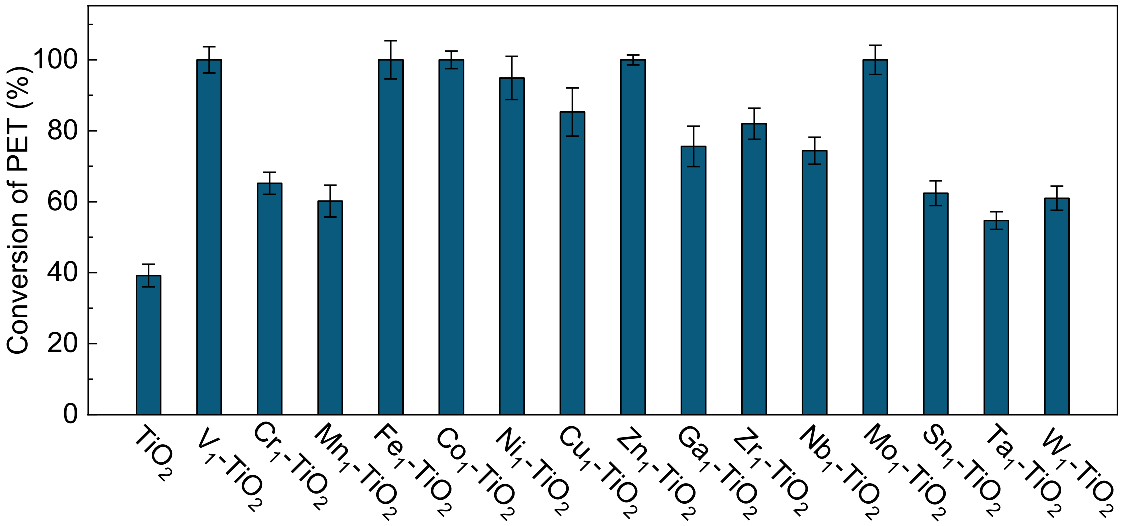

Supplementary Fig. 46 The catalytic performance of M_1-TiO_2 nanostructures for photothermal catalytic poly(ethylene terephthalate) (PET) plastic upcycling. 20 mg of M_1-TiO_2 catalysts, 2 g of ethylene glycol and 0.5 g of PET flakes were added to a sealed quartz reactor with a thermocouple inserted to maintain a temperature of 190 ^{o}C, the reaction time set at 15 min. Error bars show standard deviation between replicates (n = 3 masks for each type tested). Source data are provided as a Source Data file.

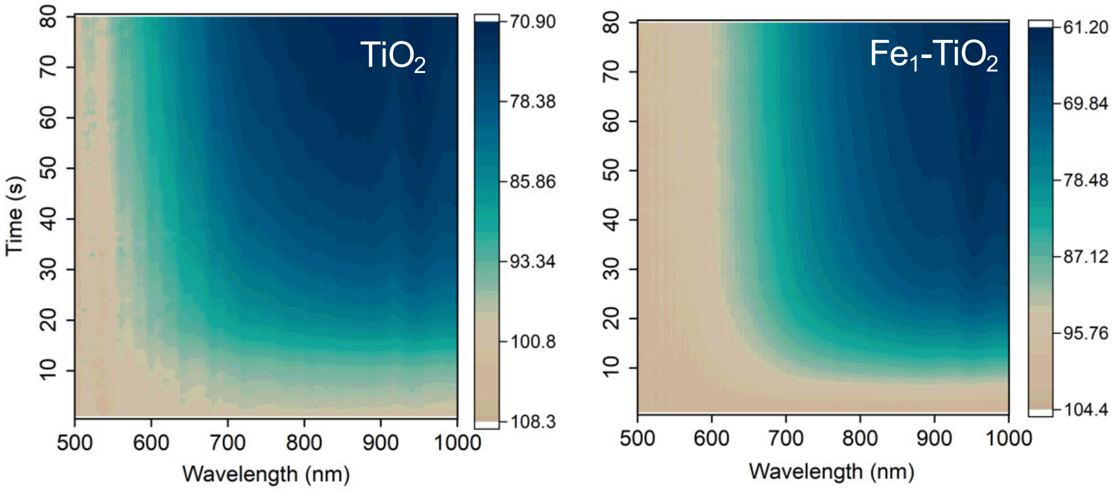

Supplementary Fig. 47 Plot of the relationship between the transmittance of the TiO_2 and Fe_1-TiO_2 disperse solution and time and wavelength. Source data are provided as a Source Data file.

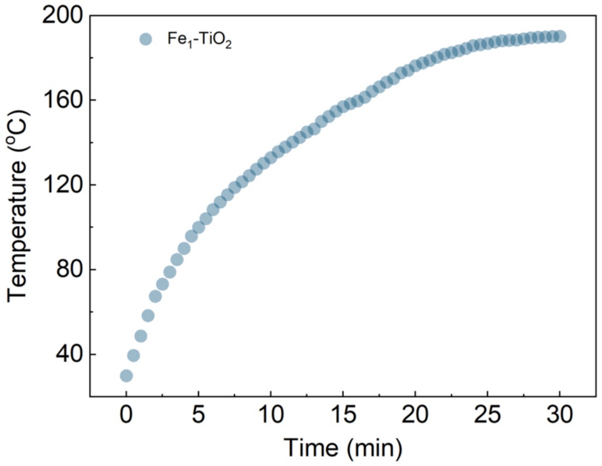

Supplementary Fig. 48 Photothermal conversion ability of Fe_1-TiO_2 dispersion. Temperature curve of the ethylene glycol solution containing 1 wt.% of Fe_1-TiO_2 shined with simulated sunlight (0.52 W·cm^{-2}). Source data are provided as a Source Data file.

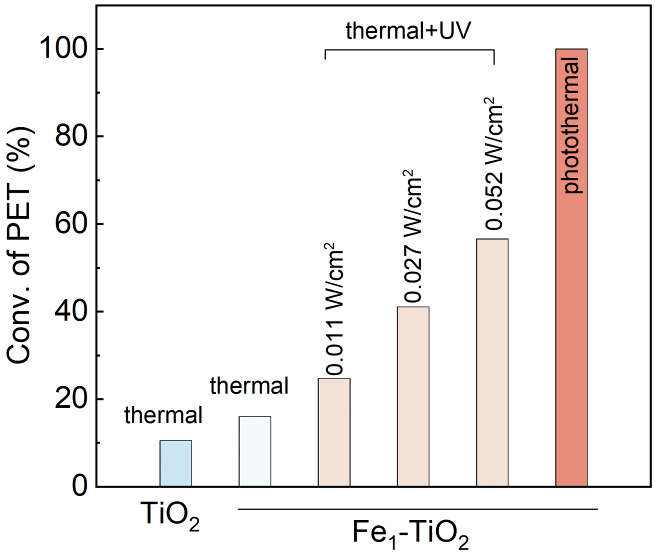

Supplementary Fig. 49 Glycolysis of poly(ethylene terephthalate) (PET) at various conditions. 20 mg of Fe_1-TiO_2 catalysts, 2 g of ethylene glycol and, 0.5 g of PET flakes were added to a sealed quartz reactor. In thermal and thermal + UV conditions the reactor was placed in an oil bath to keep a temperature of 190 °C. The UV light intensities are 0.011, 0.027 and 0.052 $W \cdot cm^{-2}$. In photothermal, the reactor was irradiation by simulated sunlight (0.52 $W \cdot cm^{-2}$). Source data are provided as a Source Data file.

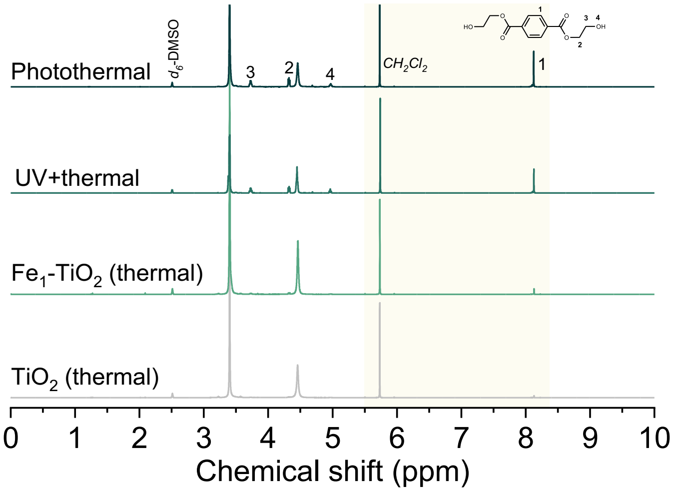

Supplementary Fig. 50 ^{1}H nuclear magnetic resonance (NMR) spectrum of the recycled product at various conditions. Source data are provided as a Source Data file.

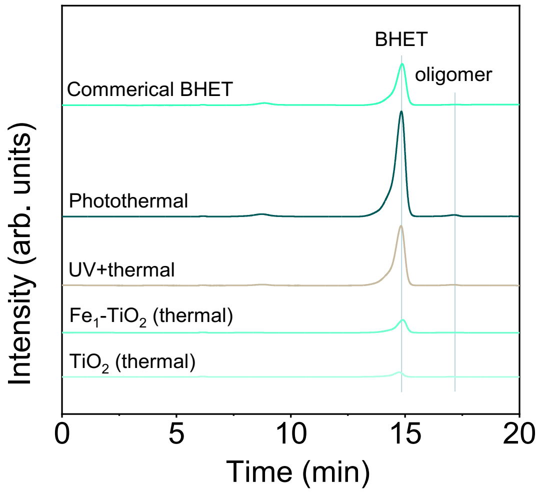

Supplementary Fig. 51 High performance liquid chromatography (HPLC) spectrum of the recycled product at various conditions. Source data are provided as a Source Data file.

The yield of bis(2-hydroxyethyl) terephthalate (BHET) was further analyzed using a Dionex HPLC-U3000 equipped with a C18 column (5 μm, 250 × 4.6 mm^2, Agilent) and an ultraviolet detector set at 254 nm. The mobile phase, a mixture of methanol and water (v/v = 50/50) was run for a duration of 20 min at a temperature of 30 °C, with a flow rate of 0.4 mL min^{-1} and an injection volume of 15 μL. The high-performance liquid chromatography (HPLC) spectrum of our product is consistent with the commercial BHET peak positions and the product contains only a small amount of oligomers.

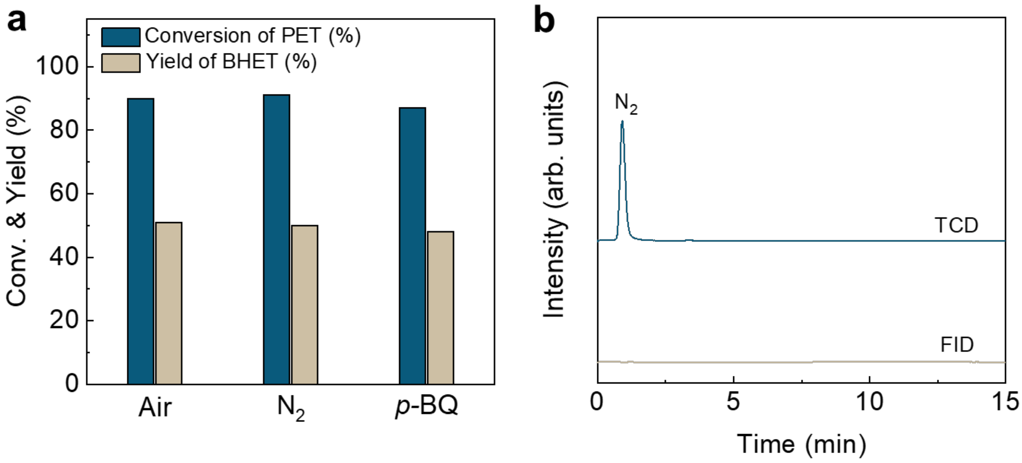

Supplementary Fig. 52. (a) Effect of reaction atmosphere and quenching agent on catalytic performance of Fe_1-TiO_2 catalysts. 20 mg of Fe_1-TiO_2 catalysts, 10 mg of *p*-benzoquinone (*p*-BQ), 2 g of ethylene glycol and 0.5 g of poly(ethylene terephthalate) (PET) flakes were added to a sealed quartz reactor with a thermocouple inserted to maintain a temperature of 190 °C, the reaction time set at 12.5 min. (b) Gas chromatography (GC) of gas-phase after photothermal catalysis in an oxygen atmosphere. Source data are provided as a Source Data file.

To further investigate the impact of oxygen on the catalytic glycolysis process, experiments were conducted under both air and nitrogen atmospheres to assess differences in poly(ethylene terephthalate) (PET) conversion and monomer yield. As shown in **a**, the results under a nitrogen are similar to those observed under ambient air conditions. Gas samples extracted during the experiments were analyzed using gas chromatography, which revealed the absence of any carbon-based compounds (**b**). This result preliminarily rules out the contribution of reactive oxygen species. Additionally, we used *p*-benzoquinone (*p*-BQ) as a quenching agent for superoxide radicals to further investigate their potential impact. The addition of *p*-BQ had not affect the catalytic activity or product selectivity (**a**), further ruling out the contribution of reactive oxygen species.

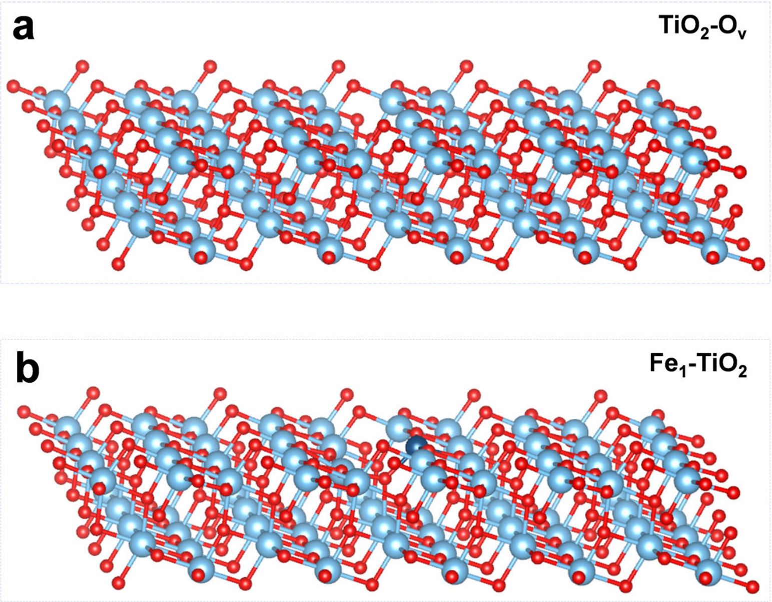

Supplementary Fig. 53 Schematic illustration of the construction of the (a) TiO_2-O_v and (b) Fe_1-TiO_2 structure model. Atom key: Ti (light blue), Fe (navy) and O (red).

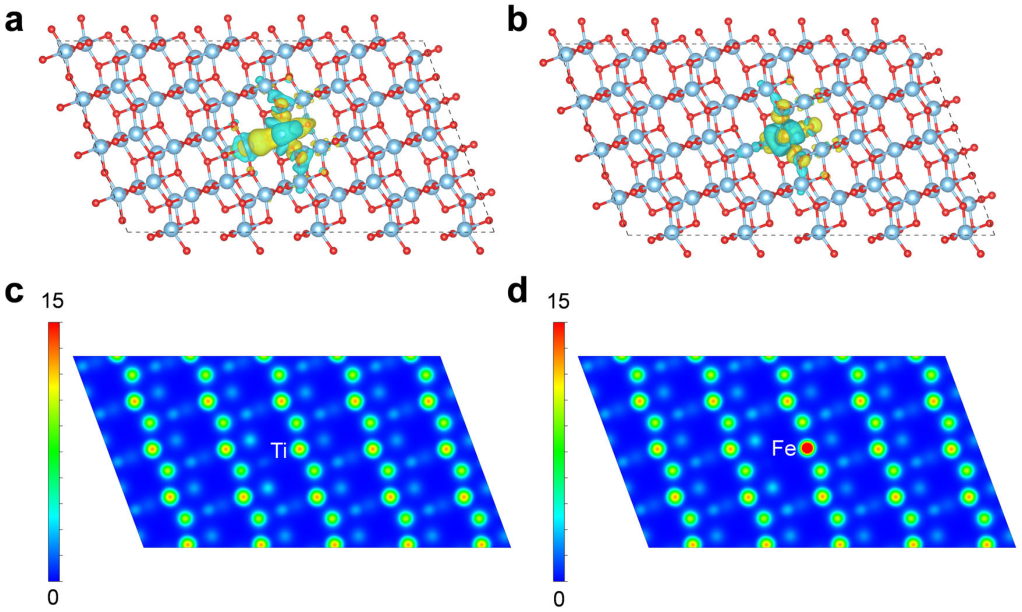

Supplementary Fig. 54 The charge density distribution of TiO_2-O_v and Fe_1-TiO_2 slabs. 3D charge density for (a) TiO_2-O_v and (b) Fe_1-TiO_2, in which the iso-surfaces are 0.003 e Bohr^{-3}. Atom key: Ti (light blue), Fe (navy) and O (red). 2D charge density for (c) TiO_2-O_v and (d) Fe_1-TiO_2.

The charge distribution is visually represented through color-coded electron clouds in these figures. Yellow regions indicate areas of increased charge density, which accumulate around the Fe and Ti atoms following the formation of oxygen vacancies. Conversely, cyan regions signify areas of decreased electron cloud density, typically observed in areas distant from the oxygen vacancies.

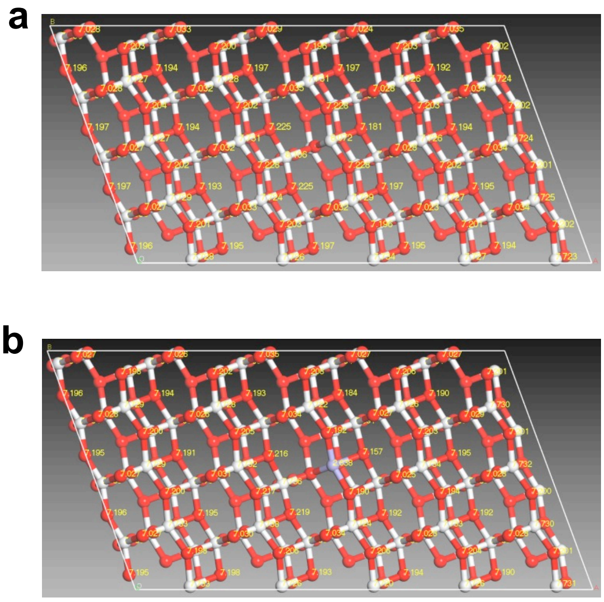

Supplementary Fig. 55 Calculated Bader charge of (a) TiO_2-O_v and (b) Fe_1-TiO_2 slabs. Atom key: Ti (white), Fe (light purple) and O (red).

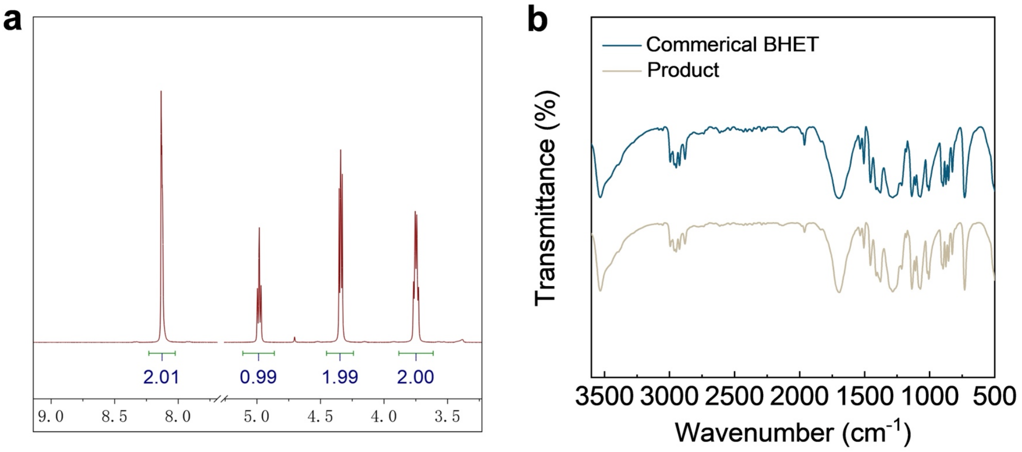

Supplementary Fig. 56 (a) ^{1}H nuclear magnetic resonance (NMR) spectrum and (b) fourier-transform infrared (FT-IR) spectrum of the recycled BHET. Source data are provided as a Source Data file.

We utilized the integration of the peaks in the ^{1}H nuclear magnetic resonance (NMR) spectrum for product quantitative analysis. As shown in **a**, the single signal observed at δ 8.1 ppm corresponds to the four symmetric aromatic protons of the benzene ring. Additionally, the triplet peak at δ 4.3 ppm and the quartet peak at δ 3.7 ppm represent the methylene protons of COO-CH_2 and CH_2-OH, respectively. The triplet peak at δ 4.9 ppm indicates the presence of protons from the hydroxyl group. The peak area ratio of these peaks (2.01:0.99:1.99:2.00) aligns with the theoretical value (2.00:1.00:2.00:2.00), Furthermore., the fourier transform-infrared (FT-IR) spectra of our products overlap well with commercial bis(2-hydroxyethyl) terephthalate (BHET) (**b**), again suggesting the high purity of the product.

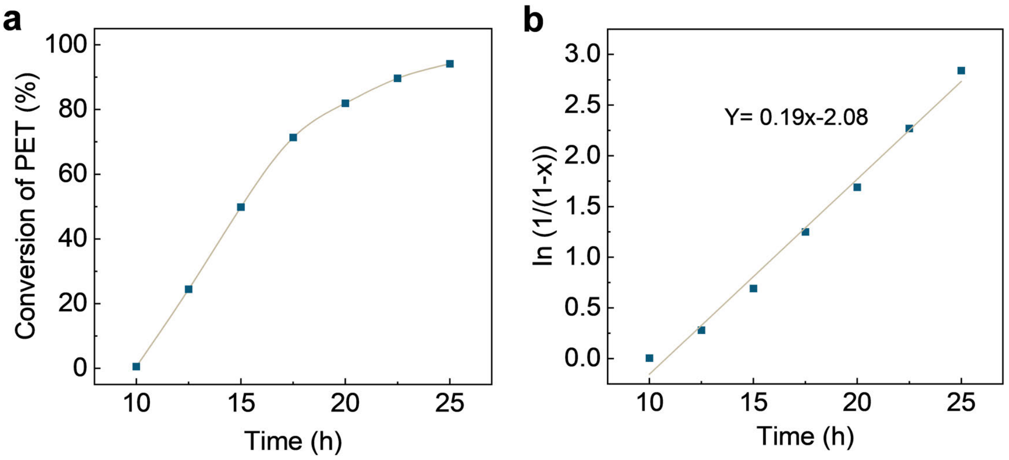

Supplementary Fig. 57 (a) The conversion of poly(ethylene terephthalate) (PET) at different times and (b) The linear fit to the PET conversion versus reaction time of Fe_1-TiO_2 nanostructures. 2 mg of Fe_1-TiO_2 catalysts, 20 g of ethylene glycol and 10 g of PET flakes were added to a sealed quartz reactor with a thermocouple inserted to maintain a temperature of 170 ^{o}C, the reaction time set at 10 hours, 12.5 hours, 15 hours, 17.5 hours, 20 hours, 22.5 hours and 25 hours, respectively. Source data are provided as a Source Data file.

We carried out seven long-term parallel experiments, aiming to simulate extended reaction periods. Each experiment maintained consistency in terms of the number of reactants (10 g poly(ethylene terephthalate) (PET) and 20 g ethylene glycol (EG)), catalyst dosage (2 mg Fe-TiO_2), light intensity (0.68 $W\cdot cm^{-2}$), and reaction temperature (170 °C). The sole parameter that varied was the reaction time, set at 10 hours, 12.5 hours, 15 hours, 17.5 hours, 20 hours, 22.5 hours and 25 hours, respectively. Notably, to accommodate longer reaction times, we reduced the catalyst dosage to 2 mg while keeping other conditions consistent with the typical reaction conditions. In **a**, we present the relationship between the conversion rate and reaction time for the seven parallel experiments. The gradual increase in the conversion rate of PET with increasing reaction time is evident. Following the literature, PET glycolysis is typically a first-order reaction. The linear fit of the data from **a** demonstrates a perfect linear relationship (**b**), indicating that the catalyst's activity remains robust even under prolonged illumination. This observation assures us of the catalyst's excellent stability over extended reaction times.

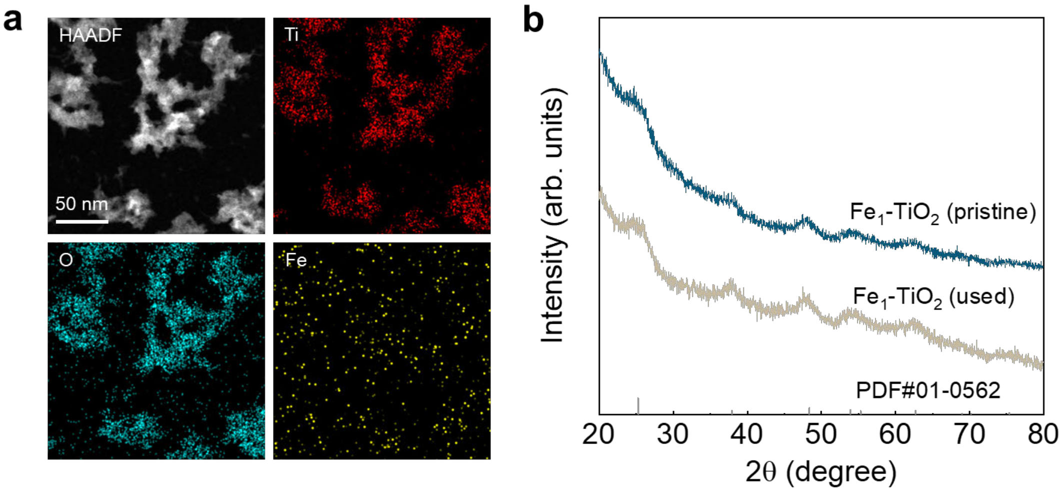

Supplementary Fig. 58 (a) Elemental mappings and (b) X-ray diffraction (XRD) patterns of Fe_1-TiO_2 nanostructures after 25 h reaction. Source data are provided as a Source Data file.

The structure of the spent Fe_1-TiO_2 catalysts were further characterized. As depicted in above figure, no distinct Fe-related species in the X-ray diffraction (XRD) patterns, coupled with the uniform distribution of Fe elements in energy dispersive X-ray spectroscopy (EDX) mapping, both confirmed no aggregation of Fe species.

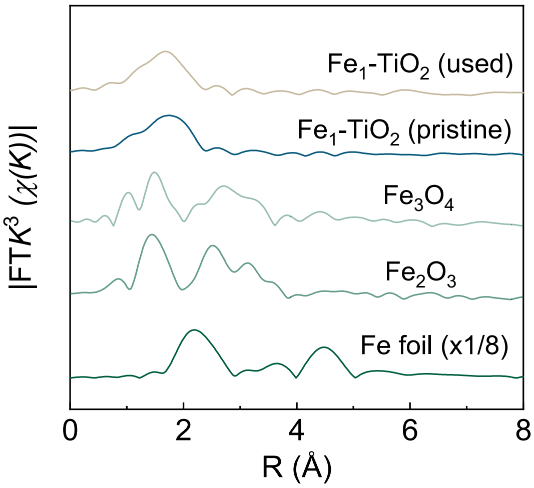

Supplementary Fig. 59 Normalized fourier transforms of the extended X-ray absorption fine structure (FT-EXAFS) spectra of pristine and used Fe$_1$-TiO$_2$. Source data are provided as a Source Data file.

Fourier transforms of the extended X-ray absorption fine structure (FT-EXAFS) analysis of the spent Fe$_1$-TiO$_2$ catalysts indicates that the Fe atoms were exclusively coordinated with oxygen atoms, evidenced by a prominent peak of Fe-O scattering at approximately 1.57 Å. Notably, no Fe-Fe peak was detected at approximately 2.18 Å, confirming that the Fe single atoms were maintained within the spent Fe$_1$-TiO$_2$ catalysts. These findings collectively affirm the exceptional stability of the Fe$_1$-TiO$_2$ nanostructures following the polyester upcycling reaction.

Supplementary Table 1 The E_0 value of the X-ray absorption near-edge structure (XANES) results for all samples.

Sample	**Threshold engergy (E_0, eV)**
TiO_2	4983.1
Fe_1-TiO_2	4980.4
Fe foil	7112.0
Fe_1-TiO_2	7122.5
Fe_3O_4	7121.7
Fe_2O_3	7123.5
Cu in $Fe_1Co_1Cu_1$-TiO_2	8985.6
CuO	8987.2
Co in $Fe_1Co_1Cu_1$-TiO_2	7718.9
Co_3O_4	7719.1
Fe in $Fe_1Co_1Cu_1$-TiO_2	7121.4
Fe in Fe_1Mo_1-TiO_2	7124.5
Mo in Fe_1Mo_1-TiO_2	20016.1
Mo foil	20000.0
MoO_3	20016.1
Ni-TiO_2	8345.8
NiO	8345.2

Supplementary Table 2 Comparison of the molar ratio of M to Ti in reported M_1-TiO_2 catalysts.

Catalyst	**Synthesis method**	**Universality**	**M/Ti (at.%)**
$Ni_{0.034}@TiO_2$[6]	molten salt, 500 °C under N_2 flow	No	1.73
Ni/TiO_2[7]	molten salt, 500 °C under N_2 flow	No	0.56
$CuSA/TiO_2$[8]	calcination, 450 °C	No	1.91
Cr_1/TiO_2[9]	calcination, 400 °C	No	1.27
Cu_1/TiO_2[10]	calcination, 950 °C	No	1.42
Cu_1/TiO_2[11]	calcination, 900 °C	Yes	0.78
Fe_1-TiO_2 (This work)	**220 °C in air**	**Yes**	**3.87**

Supplementary Table 3 The extended X-ray absorption fine structure (EXAFS) fitting results in R space at Fe K-edge.

Sample	Scattering path	CN	R (Å)	σ^2 (10^{-3}·Å^2)	ΔE_0 (eV)
Fe foil	Fe-Fe$_1$	8	2.46 ± 0.02	5.83 ± 2.03	5.01 ± 2.74
	Fe-Fe$_2$	6	2.84 ± 0.01	5.30 ± 2.75	5.01 ± 2.74
Fe$_3$O$_4$	Fe-O$_1$	4	2.04 ± 0.02	7.96 ± 3.27	8.89 ± 1.72
	Fe-O$_2$	2	2.35 ± 0.04	8.04 ± 4.58	8.89 ± 1.72
	Fe-Fe$_1$	6	3.08 ± 0.02	14.8 ± 2.85	8.89 ± 1.72
	Fe-Fe$_2$	4	3.55 ± 0.02	9.57 ± 3.27	8.89 ± 1.72
CuO	Cu-O	4	1.96 ± 0.02	3.75 ± 3.60	8.36 ± 2.14
	Cu-Cu	4	2.95 ± 0.03	9.31 ± 3.97	8.36 ± 2.14
Co$_3$O$_4$	Co-O$_1$	2	1.93 ± 0.06	4.00	2.95 ± 1.58
	Co-O$_2$	4	1.90 ± 0.05	9.24	2.95 ± 1.58
	Co-Co$_1$	4	2.87 ± 0.01	3.00	2.95 ± 1.58
	Co-Co$_2$	2	3.22 ± 0.08	4.09	2.95 ± 1.58
	Co-Co$_3$	2	3.34 ± 0.02	3.67 ± 1.25	2.95 ± 1.58
	Co-Co$_4$	4	3.44 ± 0.04	3.00	2.95 ± 1.58
MoO$_3$	Mo-O$_1$	1	1.74 ± 0.03	3.00	2.95 ± 1.58
	Mo-O$_2$	1	1.68 ± 0.02	3.00	2.95 ± 1.58
	Mo-O$_3$	2	1.96 ± 0.01	3.00	2.95 ± 1.58
	Mo-O$_4$	1	2.20 ± 0.02	3.00	2.95 ± 1.58
	Mo-O$_5$	1	2.33 ± 0.02	3.00	2.95 ± 1.58
	Mo-Mo$_1$	2	3.41 ± 0.02	3.47 ± 1.65	2.95 ± 1.58
	Mo-O$_6$	4	3.38 ± 0.05	10.1 ± 6.91	2.95 ± 1.58
	Mo-Mo$_2$	2	3.80 ± 0.01	6.57 ± 6.41	2.95 ± 1.58
	Mo-O$_7$	2	3.89 ± 0.10	3.00	2.95 ± 1.58
	Mo-Mo$_3$	2	4.03 ± 0.03	3.00	2.95 ± 1.58
Mo foil	Mo-Mo$_1$	8	2.72 ± 0.01	3.58 ± 1.64	3.37 ± 1.92
	Mo-Mo$_2$	6	3.13 ± 0.01	3.33 ± 2.19	3.37 ± 1.92
NiO	Ni-O	6	2.09 ± 0.04	16.1 ± 7.86	0.40 ± 2.88
	Ni-Ni	6	2.96 ± 0.02	3.58 ± 2.29	0.40 ± 2.88
Fe in Fe$_1$Co$_1$Cu$_1$-TiO$_2$	Fe-O	3.29 ± 1.53	2.15 ± 0.05	6.12 ± 9.60	8.91 ± 4.22
Co in Fe$_1$Co$_1$Cu$_1$-TiO$_2$	Co-O	3.38 ± 1.06	2.12 ± 0.04	3.55 ± 5.67	18.5 ± 2.9
Cu in Fe$_1$Co$_1$Cu$_1$-TiO$_2$	Cu-O	3.50 ± 1.06	2.01 ± 0.08	6.00	25.2 ± 14.9
Fe in Fe$_1$Mo$_1$-TiO$_2$	Fe-O	3.69 ± 0.72	2.03 ± 0.03	6.10 ± 3.74	1.21 ± 2.15
Mo in Fe$_1$Mo$_1$-TiO$_2$	Mo-O$_1$	2.32 ± 0.41	1.72 ± 0.05	4.78	0 ± 10.65
	Mo-O$_2$	0.69 ± 0.83	2.06 ± 0.14	6.59	0 ± 10.65
	Mo-O$_3$	1.06 ± 1.53	2.41 ± 0.09	6.00	0 ± 10.65
Ni$_1$-TiO$_2$	Ni-O	6.35 ± 1.20	2.12 ± 0.02	12.2 ± 4.2	4.34 ± 1.72
Fe$_1$-TiO$_2$	Fe-O	3.33 ± 0.40	2.07 ± 0.03	4.00	8.74 ± 2.46

CN: coordination number; R: interatomic distance; σ^2: Debye-Waller factor; ΔE_0: energy deviation; S_0^2: Amplitude reduction factor. ($S_0^2 = 0.90$)

Supplementary Table 4 Comparison of catalytic performance of reported catalysts for the glycolysis of poly(ethylene terephthalate) (PET).

Catalyst	**Catalyst amount (g)**	**PET (g)**	**Time (h)**	**BHET Yield (%)**	**STY @ 190 °C ($g_{BHET}\cdot g_{Cat.}^{-1}\cdot h^{-1}$)**
$Zn(Ac)_2$[12]	0.29	30	1	68.0	93.06
$ZnFe_2O_4$[13]	0.20	5	6	79.5	4.38
OPA@Fe_3O_4[14]	0.048	0.48	1.5	91.0	8.03
Fe_3O_4@SiO_2@(mim)[$FeCl_4$][15]	0.015	0.1	24	50.0	0.18
Zinc plates[16]	2	5	5	77.7	0.51
Zn-BDC[17]	0.06	6	3	87.3	38.49
SiO_2-Fe_2O_3-NH_2SB NP[18]	0.1	1	3	73.0	3.22
[Ch][OAc][19]	0.25	5	3	83.8	7.39
t-BuP_2[20]	0.25	0.5	1.5	92.7	1.64
4Ti/SBA-15[21]	0.05	0.4	3/4	87.2	12.30
Fe_3O_4-CP NPs[22]	0.01	1	2	56.9	37.64
ZnO-Fe_3O_4 HMNAs[23]	0.5	1.5	0.5	92.3	7.33
$Zn(OAc)_2$[24]	0.5	1.5	1/12	83.0	38.75
MeONa[25]	0.28	1	2	75.0	1.77
[HDBU]Im[26]	0.25	5	2/3	78.9	31.16
Cyanamide[27]	0.1	2	2.5	95.2	10.08
MAF-6[28]	0.05	5	4	78.3	25.89
$ZnCl_2$[29]	1	5	2	81.1	2.68
$CoCl_2$[29]	1	5	2	72.7	2.40
Mo/ZnO[30]	0.01	1	1	92.3	122.11
GCNC[31]	0.05	2	0.5	75.0	79.38
[Bmim]HCO_3[32]	0.1	2	2	71.2	9.42
1,3-DMU/$Zn(OAc)_2$[33]	0.25	5	1/3	82.0	65.75
rGO/$[TESPMI]_2CoCl_4$[34]	0.15	1	3	87.3	2.57
$NaHCO_3$[35]	0.25	5	3	48.0	4.23
Fe_1-TiO_2 (This work)	0.02	0.5	1/4	76.2	**100.81**

Supplementary Table 5 Total energy and free energy correction for molecules and reaction intermediates over TiO_2-O_v and Fe_1-TiO_2 slabs for photothermal catalytic poly(ethylene terephthalate) (PET) glycolysis.

Intermediates	**E_{DFT} (eV)**	**E_{ZPE} (eV)**	**TΔS (eV)**
Ethylene glycol (EG)	-53.17	2.24	0.94
Ethylene glycol dibenzoate (EGD)	-222.57	7.11	0.94
2-hydroxyethyl benzoate (2-HB)	-137.87	4.67	1.39
TiO_2-O_v	-1855.52	/	/
IS1* on TiO_2-O_v	-2078.99	7.13	0.86
IS2* on TiO_2-O_v	-2132.25	9.40	1.26
IS3* on TiO_2-O_v	-1994.51	4.71	0.67
Fe_1-TiO_2	-1852.24	/	/
IS1* on Fe_1-TiO_2	-2075.79	7.16	0.74
IS2* on Fe_1-TiO_2	-2128.97	9.41	1.28
IS3* on Fe_1-TiO_2	-1991.03	4.72	0.52

Supplementary Table 6 Mass of metal chloride precursors required for the synthesis of M_1-TiO_2 nanostructures.

Materials	Metal chloride	Mass (mg)
V_1-TiO_2	VCl_3	28.31
Cr_1-TiO_2	$CrCl_3$	28.50
Mn_1-TiO_2	$MnCl_2$	22.65
Fe_1-TiO_2	$FeCl_3$	29.20
15% Fe_1-TiO_2	$FeCl_3$	87.60
Co_1-TiO_2	$CoCl_2\cdot 6H_2O$	42.83
Ni_1-TiO_2	$NiCl_2\cdot 6H_2O$	42.78
Cu_1-TiO_2	$CuCl_2$	24.20
Zn_1-TiO_2	$ZnCl_2$	24.54
Ga_1-TiO_2	$GaCl_3$	31.69
Zr_1-TiO_2	$ZrCl_2$	41.95
Nb_1-TiO_2	$NbCl_5$	48.63
Mo_1-TiO_2	$MoCl_5$	49.18
Sn_1-TiO_2	$SnCl_4\cdot 5H_2O$	63.11
Ta_1-TiO_2	$TaCl_5$	64.48
W_1-TiO_2	WCl_6	71.39
Fe_1Mo_1-TiO_2	$FeCl_3$	14.60
	$MoCl_5$	24.59
$Fe_1Co_1Cu_1$-TiO_2	$FeCl_3$	9.73
	$CoCl_2\cdot 6H_2O$	14.28
	$CuCl_2$	8.07
Ru-TiO_2	$RuCl_3$	37.75
Rh-TiO_2	$RhCl_3$	38.08
Pd-TiO_2	$PdCl_2$	32.27
Ir-TiO_2	$IrCl_3\cdot 3H_2O$	64.17

References

[1] Kresse, G. & Furthmiiller, J. Efficiency of ab-initio total energy calculations for metals and semiconductors using a plane-wave basis set. *Comput. Mater. Sci.* **6**, 15–50 (1996).

[2] Perdew, J. P., Burke, K. & Ernzerhof, M. Generalized gradient approximation made simple. *Phys. Rev. Lett.* **77**, 3865 (1996).

[3] Grimme, S., Antony, J., Ehrlich, S. & Krieg, H. A consistent and accurate ab initio parametrization of density functional dispersion correction (DFT-D) for the 94 elements H-Pu. *J. Chem. Phys.* **132**, 154104 (2010).

[4] Wang, L., Maxisch, T. & Ceder, G. Oxidation energies of transition metal oxides within the GGA+U framework. *Phys. Rev. B* **73**, 195107 (2006).

[5] Aykol, M. & Wolverton, C. Local environment dependent GGA+U method for accurate thermochemistry of transition metal compounds. *Phys. Rev. B* **90**, 115105 (2014).

[6] Zhang, J. et al. Single-atom Ni supported on TiO_2 for catalyzing hydrogen storage in MgH_2. *J. Am. Chem. Soc.* **146**, 10432–10442 (2024).

[7] Xiao, M. et al. Molten-salt-mediated synthesis of an atomic nickel Co-catalyst on TiO_2 for improved photocatalytic H_2 evolution. *Angew. Chem. Int. Ed.* **59**, 7230–7234 (2020).

[8] Zhang, Y. et al. Single-atom Cu anchored catalysts for photocatalytic renewable H_2 production with a quantum efficiency of 56%. *Nat. Commun.* **13**, 58 (2022).

[9] Shen, Q. et al. Single chromium atoms supported on titanium dioxide nanoparticles for synergic catalytic methane conversion under mild conditions. *Angew. Chem. Int. Ed.* **59**, 1216–1219 (2019).

[10] Lee, B. et al. Electronic interaction between transition metal single-atoms and anatase TiO_2 boosts CO_2 photoreduction with H_2O. *Energy Environ. Sci.* **15**, 601–609 (2022).

[11] Lee, B. h. et al. Reversible and cooperative photoactivation of single-atom Cu/TiO_2 photocatalysts. *Nat. Mater.* **18**, 620–626 (2019).

[12] López-Fonseca, R., Duque-Ingunza, I., de Rivas, B., Arnaiz, S. & Gutiérrez-

Ortiz, J. I. Chemical recycling of post-consumer PET wastes by glycolysis in the presence of metal salts. *Polym. Degrad. Stab.* **95**, 1022–1028 (2010).

[13] Anggo Krisbiantoro, P. et al. Catalytic glycolysis of polyethylene terephthalate (PET) by solvent-free mechanochemically synthesized MFe_2O_4 (M = Co, Ni, Cu and Zn) spinel. *Chem. Eng. J.* **450**, 137926 (2022).

[14] Lalhmangaihzuala, S., Laldinpuii, Z. T., Khiangte, V., Lallawmzuali, G. & Thanhmingliana, V. K. Orange peel ash coated Fe_3O_4 nanoparticles as a magnetically retrievable catalyst for glycolysis and methanolysis of PET waste. *Adv. Powder Technol.* **34**, 104076 (2023).

[15] Cano, I. et al. Paramagnetic ionic liquid-coated $SiO_2@Fe_3O_4$ nanoparticles–the next generation of magnetically recoverable nanocatalysts applied in the glycolysis of PET. *Appl. Catal. B Environ.* **260**, 118110 (2020).

[16] Chiao, Y. et al. Waste-battery-derived multifunctional zinc catalysts for glycolysis and decolorization of polyethylene terephthalate. *Appl. Catal. B Environ.* **325**, 122302 (2023).

[17] Pham, D. D. et al. A new circulation in glycolysis of polyethylene terephthalate using MOF-based catalysts for environmental sustainability of plastic. *Chem. Eng. J.* **490**, 151667 (2024).

[18] Casey, É. et al. Ligand-aided glycolysis of PET using functionalized silica-supported Fe_2O_3 nanoparticles. ACS Sustain. *Chem. Eng.* **11**, 15544–15555 (2023).

[19] Liu, Y. et al. Degradation of poly(ethylene terephthalate) catalyzed by metal-free choline-based ionic liquids. *Green Chem.* **22**, 3122–3131 (2020).

[20] Fan, C. et al. Efficient glycolysis of PET catalyzed by a metal-free phosphazene base: the important role of EG^-. *Green Chem.* **24**, 1294–1301 (2022).

[21] Mo, S., Guo, Y., Liu, X. & Wang, Y. Efficient depolymerization of PET over Ti-doped SBA-15 with abundant lewis acid sites via glycolysis. *Catal. Sci. Technol.* **13**, 6561–6569 (2023).

[22] Jo, Y., Kim, E. J., Kim, J. & An, K. Efficient Fe_3O_4 nanoparticle catalysts for depolymerization of polyethylene terephthalate. *Green Chem.* **25**, 8160–8171

(2023).

[23] Yun, L. et al. Magnetic hollow micro-sized nanoaggregates for synergistically accelerating PET glycolysis. *Green Chem.* **25**, 6901–6913 (2023).

[24] Chen, Q., Wu, S., Zhang, P., Song, X. M. & Song, Z. Hot pickering emulsion interfacial catalysis accelerates polyethylene terephthalate (PET) glycolysis. *Green Chem.* **25**, 9146-9155 (2023).

[25] Javed, S. & Vogt, D. Development of eco-friendly and sustainable PET glycolysis using sodium alkoxides as catalysts. ACS Sustain. *Chem. Eng.* **11**, 11541–11547 (2023).

[26] Zhang, R. et al. Degradation of poly(ethylene terephthalate) catalyzed by nonmetallic dibasic ionic liquids under UV radiation. *Mater.* **17**, 1583 (2024).

[27] Wang, Z., Jin, Y., Wang, Y., Tang, Z., Wang, S., Xiao, G. & Su, H. Cyanamide as a highly efficient organocatalyst for the glycolysis recycling of PET. *ACS Sustain. Chem. Eng.* **10**, 7965–7973 (2022).

[28] Yang, R. X. et al. Heterogeneous metal azolate framework-6 (MAF-6) catalysts with high zinc density for enhanced polyethylene terephthalate (PET) conversion. *ACS Sustain. Chem. Eng.* **9**, 6541–6550 (2021).

[29] Wang, T., Shen, C., Yu, G. & Chen, X. Metal ions immobilized on polymer ionic liquid as novel efficient and facile recycled catalyst for glycolysis of PET. *Polym. Degrad. Stab.* **194**, 109751 (2021).

[30] Cao, J. et al. Mechanism of the significant acceleration of polyethylene terephthalate glycolysis by defective ultrathin ZnO nanosheets with heteroatom doping. *ACS Sustain. Chem. Eng.* **10**, 5476–5488 (2022).

[31] Wang, Z. et al. A pseudo-homogeneous system for PET glycolysis using a colloidal catalyst of graphite carbon nitride in ethylene glycol. *Polym. Degrad. Stab.* **190**, 109638 (2021).

[32] Yue, Q. F., Wang, C. X., Zhang, L. N., Ni, Y. & Jin, Y. X. Glycolysis of poly(ethylene terephthalate) (PET) using basic ionic liquids as catalysts. *Polym. Degrad. Stab.* **96**, 399-403 (2011).

[33] Liu, B., Fu, W., Lu, X., Zhou, Q. & Zhang, S. Lewis acid–base synergistic

catalysis for polyethylene terephthalate degradation by 1,3-dimethylurea/Zn(OAc)$_2$ deep eutectic solvent. ACS Sustain. *Chem. Eng.* **7**, 3292–3300 (2018).

[34] Najafi-Shoa, S., Barikani, M., Ehsani, M. & Ghaffari, M. Cobalt-based ionic liquid grafted on graphene as a heterogeneous catalyst for poly (ethylene terephthalate) glycolysis. *Polym. Degrad. Stab.* **192**, 109691 (2021).

[35] Pan, Y. et al. Integrating glycolysis and enzymatic catalyst to convert waste poly(ethylene terephthalate) into terephthalic acid. *Biochem. Eng. J.* **207**, 109328 (2024).